Parameterization of Shortwave and Longwave Radiative Properties of Ice Clouds for Use in Climate Models

GANG HONG AND PING YANG

Department of Atmospheric Sciences, Texas A&M University, College Station, Texas

BRYAN A. BAUM

Space Science and Engineering Center, University of Wisconsin—Madison, Madison, Wisconsin

ANDREW J. HEYMSFIELD

National Center for Atmospheric Research, Boulder, Colorado

KUAN-MAN XU

NASA Langley Research Center, Hampton, Virginia

(Manuscript received 18 September 2008, in final form 1 July 2009)

ABSTRACT

Climate modeling and prediction require that the parameterization of the radiative effects of ice clouds be as accurate as possible. The radiative properties of ice clouds are highly sensitive to the single-scattering properties of ice particles and ice cloud microphysical properties such as particle habits and size distributions. In this study, parameterizations for shortwave (SW) and longwave (LW) radiative properties of ice clouds are developed for three existing schemes using ice cloud microphysical properties obtained from five field campaigns and broadband-averaged single-scattering properties of nonspherical ice particles as functions of the effective particle size D_e (defined as 1.5 times the ratio of total volume to total projected area), which include hexagonal solid columns and hollow columns, hexagonal plates, six-branch bullet rosettes, aggregates, and droxtals.

A combination of the discrete ordinates radiative transfer model and a line-by-line model is used to simulate ice cloud radiative forcing (CRF) at both the surface and the top of the atmosphere (TOA) for the three redeveloped parameterization schemes. The differences in CRF for different parameterization schemes are in the range of -5 to 5 W m^{-2}. In general, the large differences in SW and total CRF occur for thick ice clouds, whereas the large differences in LW CRF occur for ice clouds with small ice particles (D_e less than 20 μm). The redeveloped parameterization schemes are then applied to the radiative transfer models used for climate models. The ice cloud optical and microphysical properties from the Moderate Resolution Imaging Spectroradiometer (MODIS) cloud product over a granule and the collocated atmospheric profiles from the Atmospheric Infrared Sounder (AIRS) product are input into these radiative transfer models to compare the differences in CRF between the redeveloped and existing parameterization schemes. Although differences between these schemes are small in the LW CRF, the differences in the SW CRF are quite large.

1. Introduction

Ice clouds cover about 20%–30% of the earth (e.g., Liou 1986; Rossow and Schiffer 1999; Lynch et al. 2002; Wylie et al. 2005; Hong et al. 2007b). Through their effects on the earth's radiation budget at the top of the atmosphere (TOA), within the atmosphere, and at the surface, ice clouds play an important role in the climate system (e.g., Starr and Cox 1985; Liou 1986). However, because these clouds are usually optically thin and their high altitudes pose significant difficulties for in situ measurements, particularly near convective clouds, uncertainties remain in the description of their global coverage and macrophysical, microphysical, and optical properties (e.g., Liou 1986; Starr 1987; Stephens et al.

Corresponding author address: Dr. Gang Hong, Department of Atmospheric Sciences, Texas A&M University, College Station, TX 77843.
E-mail: hong@ariel.met.tamu.edu

DOI: 10.1175/2009JCLI2844.1

© 2009 American Meteorological Society

1990; Minnis et al. 1993; Mishchenko et al. 1996; Toon and Miake-Lye 1998; Liu and Curry 1999; Baum et al. 2000a,b; Dessler and Yang 2003; Hatzianastassiou et al. 2004; Kokhanovsky and Nauss 2006). The uncertainties can be potentially mitigated by the satellite series included in A-train (Stephens et al. 2002), particularly Cloudsat and Cloud–Aerosol Lidar and Infrared Pathfinder Satellite Observation (CALIPSO), providing the vertical profiles of ice cloud properties. To better characterize the radiative effects of ice clouds in general circulation models (GCMs), parameterizations of ice cloud radiative properties need to incorporate the latest advances in both the derivation of the single-scattering properties and in situ microphysical measurements.

The development of a reliable parameterization of ice cloud radiative properties requires the fundamental scattering and absorption properties of ice particles across the spectrum from visible wavelengths through the infrared (IR). In situ measurements from various field campaigns and laboratory experiments indicate that ice particles are composed of a variety of nonspherical habits (e.g., Heymsfield and Miloshevich 2003; Bailey and Hallett 2004). The complex habits of ice crystals pose a challenge in scattering computation, because there is no exact analytical solution for the scattering and absorption by nonspherical ice particles (Liou and Takano 1994; Fu et al. 1998, hereafter FU).

Takano and Liou (1989) investigated the single-scattering properties of ice clouds composed of hexagonal columns using the geometric optics method (GOM), or the ray-tracing technique, for five solar bands. In their study, an empirical polynomial equation was used to fit the single-scattering albedo as a function of the aspect ratio of hexagonal columns and absorption coefficient. The anomalous diffraction theory (ADT) was used by Stephens et al. (1990) to develop a parameterization of solar radiative properties. The work of Takano and Liou (1989) was extended by Ebert and Curry (1992, hereafter EB), who developed a parameterization of the ice cloud optical properties using the single-scattering properties of hexagonal columns for five solar and five infrared bands as functions of effective particle size and ice water path. Fu and Liou (1993) also developed a parameterization based on hexagonal columns, but for 6 solar bands and 12 IR bands. For their parameterization, the microphysical properties were based on the mean effective particle sizes and ice water contents (IWCs) of 11 observed ice particle size distributions (PSDs). A more accurate parameterization of the solar radiative properties of ice clouds was developed by Fu (1996) based on an improved GOM (IGOM; Yang and Liou 1996a) for solid hexagonal columns in the solar spectrum. This parameterization used a larger set of 28 ice particle size distributions obtained from in situ aircraft measurements from both tropical and midlatitude regions and a generalized effective particle size. FU improved the parameterization for the IR radiative properties of ice clouds. The single-scattering calculations for solid hexagonal columns were based on a composite scheme based on the Lorenz–Mie theory, the GOM, and the finite-difference time domain technique (FDTD; Yang and Liou 1996b). Chou et al. (1999, hereafter CH99) also reported an IR parameterization of the bulk optical properties of ice clouds for their radiation transfer model.

Yang et al. (2000, 2005) computed the single-scattering properties for ice particles using six habits (hexagonal plates, solid and hollow columns, 2D and 3D bullet rosettes, and aggregates composed of solid hexagonal columns) at both solar and IR wavelengths. The solar wavelength calculations used the IGOM and FDTD, whereas the IR scattering properties were computed using a composite method based on a combination of the FDTD, IGOM, and Lorenz–Mie theory. Single-scattering properties were developed subsequently for droxtal ice crystals, which are employed to represent the small quasi-spherical particles in a size distribution (Yang et al. 2003; Zhang et al. 2004).

The single-scattering properties of these ice particles have been used for satellite- and aircraft-based retrievals of optical and microphysical properties of ice clouds (e.g., Platnick et al. 2003; Huang et al. 2004; Gao et al. 2004; Meyer et al. 2004; King et al. 2004, 2006; Li et al. 2005; Yang et al. 2005; Baum et al. 2005a,b; Wei et al. 2004; Wendisch et al. 2005, 2007; Hong et al. 2007a). However, there is relatively little recent research documenting the use of these ice particles to develop a parameterization of the solar and infrared radiative properties for use in GCMs.

Parameterizations of the shortwave (SW) radiative properties for seven ice particle shapes, including solid and hollow hexagonal columns, hexagonal plates, 2D and 3D bullet rosettes, aggregates, and dendrites, were developed individually by Key et al. (2002) using 6, 24, and 56 bands from 0.2 to 5 μm. Chou et al. (2002, hereafter CH02) developed parameterizations for the SW radiative properties of ice clouds based on the single-scattering database from Yang et al. (2000) and the 30 particle size distributions used by Fu (1996) and Mitchell and Arnott (1994). However, these parameterizations used the same habit mixture used for the early Moderate Resolution Imaging Spectroradiometer (MODIS) cloud products (collections 1–4) and also the habit mixture developed for tropical cirrus clouds by McFarquhar et al. (2002). For ice clouds, Yang et al. (2005) parameterized IR scattering properties, assuming the same habit mixture that was used for the operational MODIS (collection 4) cloud retrieval,

for 49 wavelengths and for the 21 particle size distributions used in Fu (1996). In the aforementioned broadband parameterizations of ice cloud radiative properties, only 30 ice cloud particle size distributions were used.

Baum et al. (2005a) derived particle habit mixtures based on aircraft in situ data obtained from midlatitude and tropical ice clouds, which included more than 1100 ice cloud PSDs. Each of the PSDs included IWC and median mass diameters D_{mm}. These ice cloud microphysical properties were then merged with the single-scattering properties of nonspherical ice particles from Yang et al. (2000, 2005) to develop scattering models for application to use with satellite remote sensing (Baum et al. 2005b, 2007).

Besides applying the abundant ice cloud microphysical data and the single-scattering properties of nonspherical ice particles for use with satellite remote sensing applications, it is necessary to involve them in general circulation models and climate models to improve simulations. The parameterizations of ice cloud radiative properties, which have been developed by EB, Fu and Liou (1993), Fu (1996), FU, Key et al. (2002), CH99, and CH02, have been extensively used in GCMs (e.g., Kiehl et al. 1998; Lubin et al. 1998; Morcrette and Jakob 2000; Oreopoulos et al. 2004, 2009). The main objective of this study is to revisit the parameterizations for both the SW and longwave (LW) radiative properties of ice clouds and to update the parameterizations using the newly available single-scattering properties of ice particles and an expanded set of microphysical measurements. The single-scattering properties of nonspherical ice particles and the particle size distributions of ice clouds measured from several field campaigns are introduced in section 2. The single-scattering properties of ice particles are averaged over the measured particle size distributions to obtain the cloud bulk scattering properties, which are then parameterized as a function of effective particle size in section 3. Section 4 presents the comparison of SW and LW cloud forcing among the redeveloped schemes. The effect of habit mixtures of ice particles on the parameterization is also investigated. In section 5, the redeveloped parameterizations are used to investigate the cloud radiative forcing (CRF) using the ice cloud optical and microphysical retrievals from MODIS and the atmospheric profiles retrieved from the Atmospheric Infrared Sounder (AIRS). Finally, the results are summarized in section 6.

2. Ice particle single-scattering and microphysical properties

a. Single-scattering properties of nonspherical ice particles

Various techniques have been developed to calculate the single-scattering properties of nonspherical ice particles [see reviews by Mishchenko et al. (2002), Baran (2004), and Kokhanovsky (2006)]. Among these models are the GOM (Takano and Liou 1989; Macke et al. 1996; Yang and Liou 1996a), the T-matrix method (Mishchenko et al. 1996, 2000), the FDTD (Yee 1966; Yang and Liou 1996b; Sun et al. 1999), the discrete dipole approximation method (DDA; Draine and Flatau 1994; Yurkin et al. 2007), and other methods (Mitchell 2002).

The T-matrix method, which is generally applied to axially symmetric particles, is a computationally efficient approach for computing the optical properties of particles with small and moderate size parameters. The FDTD and DDA are applicable to arbitrarily shaped inhomogeneous particles, but for size parameters smaller than the counterparts of regarding of the applicability of the T-matrix method. The GOM is applicable to arbitrarily shaped inhomogeneous particles, but it is limited to particles with a relatively large size parameter.

Ice clouds are composed of particles with complex shapes that depend on temperature, humidity, and vertical wind speed (e.g., Heymsfield and Miloshevich 2003; Bailey and Hallett 2004). The scattering properties are highly sensitive to ice particle habits (e.g., Macke et al. 1998; Wyser and Yang 1998; Yang et al. 2000, 2005). It is impractical to compute the single-scattering properties of all possible habits. A common approach is to choose some typical habits to represent those in ice clouds. By combining the IGOM and FDTD (Yang and Liou 1996a,b), comprehensive libraries of the single-scattering properties of ice particles have been developed over a range of wavelengths from 0.2 to 100 μm for six habits, including droxtals, hexagonal solid columns, hollow columns, plates, bullet rosettes, and aggregates (Yang et al. 2000, 2005). Particle sizes, in terms of maximum dimension D_{max}, range from 2 to 9500 μm. Only the aggregate, consisting of hexagonal solid columns, has rough surface in the numerical calculations; the other particles have smooth faces. The libraries include particle volume V and projected area A in addition to the scattering properties, including extinction efficiency Q_{ext}, single-scattering albedo ω, asymmetry factor g, scattering phase function $P(\theta)$ (where θ is the scattering angle), and δ-function transmission as functions of particle maximum dimension and wavelength.

Figure 1 shows the contours of the extinction efficiency, absorption efficiency, and asymmetry factor as functions of wavelength and maximum dimension for hexagonal solid columns and plates. The single-scattering properties are found to be sensitive to the incident wavelength, particle size, and habit. The absorption efficiency, which is strongly related to the imaginary part of the refractive index of ice, is quite large in the IR. The extinction efficiency is relatively small for small ice particles

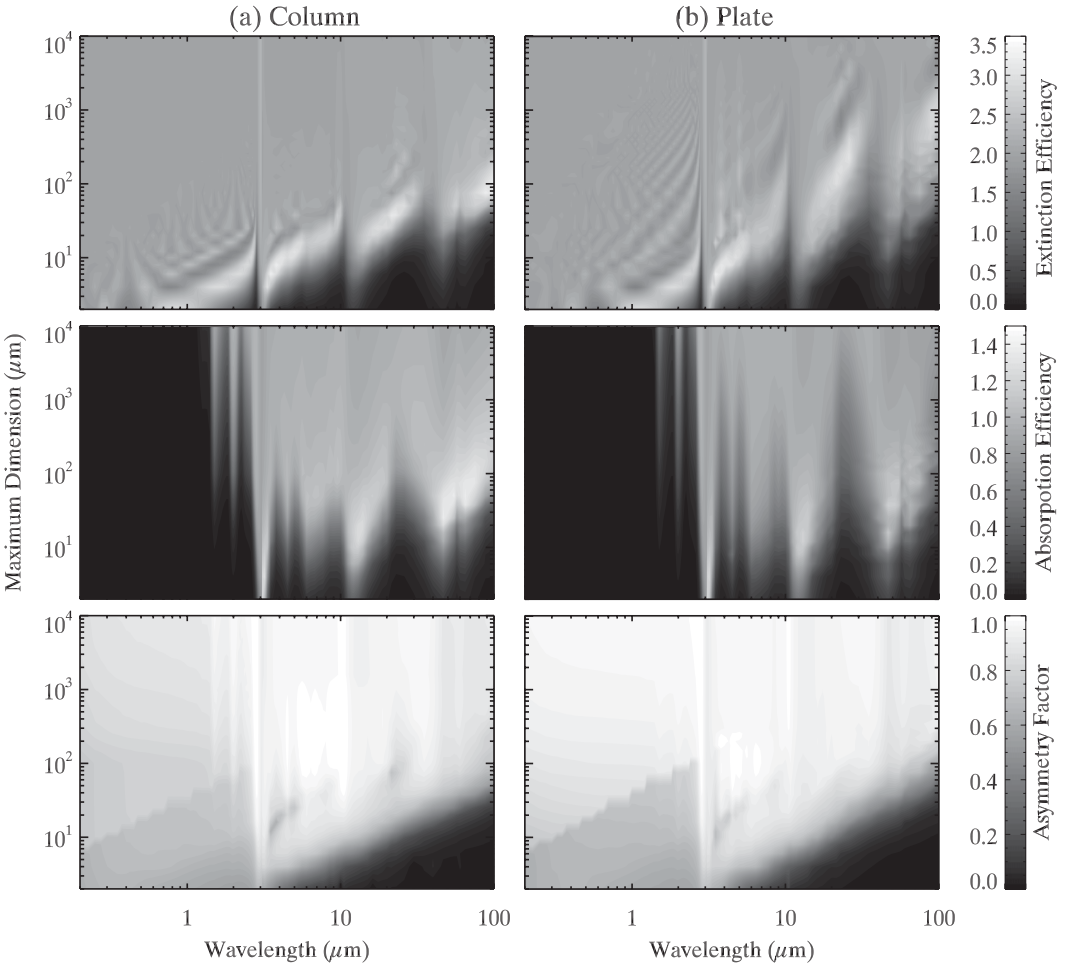

FIG. 1. The extinction efficiency, absorption efficiency, and asymmetry factor as functions of wavelength ranging from 0.2 to 100.0 μm and maximum dimension ranging from 2.0 to 9500.0 μm for (a) solid columns and (b) plates.

in the IR. In the IR, the asymmetry factor has low values when particle sizes are small.

b. Particle size distributions

A set of 1119 PSDs that were derived from in situ measurements in both tropical and midlatitude regions is used in this study. This is the same set of PSDs described in Baum et al. (2005a); further information is provided in Table 1. The tropical measurements are from two campaigns conducted in Kwajalein, Marshall Islands, in 1999 under the auspices of the Tropical Rainfall Measuring Mission (TRMM; Stith et al. 2002, 2004) and the Cirrus Regional Study of Tropical Anvils and Cirrus Layers (CRYSTAL) Florida Area Cirrus Experiment (FACE) in 2002. The midlatude measurements include the First International Satellite Cloud Climatology Project Regional Experiments (FIRE-I) in Madison, Wisconsin, in 1986; FIRE-II in Coffeyville, Kansas, in 1991; and the Atmospheric Radiative Measurement Program (ARM) near Lamont, Oklahoma, in 2000. Further details of the microphysical measurements are provided by Miloshevich and Heymsfield (1997), Heymsfield et al. (2002, 2003, 2004), Heymsfield and Miloshevich (2003), and Baum et al. (2005a).

Each PSD is described by a gamma distribution (e.g., Kosarev and Mazin 1991; Mitchell 2002; Heymsfield et al. 2002; Baum et al. 2005a) in the form

$$N(D) = N_0 D^{\mu} e^{-\lambda D}, \tag{1}$$

where N_0 is the intercept, λ is the slope, μ is the dispersion, $N(D)$ is the particle concentration per unit volume, and D is the diameter of the ice particle. In addition to the set of 1119 particle size distributions, an

TABLE 1. Number of ice crystal PSDs for each field campaign.

Field campaign	Location and time	No. of total PSDs	No. of filtered PSDs
TRMM	Kwajalein, Marshall Islands, 1999	1133	418
CRYSTAL-FACE	Nicaragua/Caribbean, 2002	42	42
FIRE-I	Madison, WI, 1986	479	247
FIRE-II	Coffeyville, KS, 1991	23	22
ARM	Lamont, OK, 2000	390	390

additional set of 21 PSDs used in Fu (1996) are included in the present study; these additional PSDs supplement the information for PSDs with very small particles. Thus, there is a total of 1140 PSDs in the set.

3. Parameterization of optical properties of ice clouds

a. Broadband-averaged bulk scattering properties

Parameterizations of ice cloud scattering properties are generally developed for fairly broad spectral bands to minimize computational costs in a GCM. For example, Fu and Liou (1993), Fu (1996), and FU built a parameterization for 6 bands in the SW region (0.2–5.0 μm) and 12 bands in the LW spectral region. CH99 and CH02 chose 11 and 12 bands for SW and LW spectra, respectively. Key et al. (2002) developed SW parameterizations for 6, 24, and 56 bands for individual ice habits.

To obtain the broadband-averaged bulk scattering properties for a given parameter in the shortwave, the single-scattering properties of ice particles are integrated over wavelength across the band as follows:

$$\langle Q_{\text{ext}}\rangle = \frac{\int_{\lambda_1}^{\lambda_2}\int_{D_{\min}}^{D_{\max}}\left[\sum_{i=1}^{N} f_i(D)Q_{\text{ext},i}(\lambda, D)A_i(D)\right]N(D)S(\lambda)\,dD\,d\lambda}{\int_{\lambda_1}^{\lambda_2}\int_{D_{\min}}^{D_{\max}}\left[\sum_{i=1}^{N} f_i(D)A_i(D)\right]N(D)S(\lambda)\,dD\,d\lambda}, \tag{2a}$$

$$\langle \omega\rangle = \frac{\int_{\lambda_1}^{\lambda_2}\int_{D_{\min}}^{D_{\max}}\left[\sum_{i=1}^{N} f_i(D)\omega_i(\lambda, D)Q_{\text{ext},i}(\lambda, D)A_i(D)\right]N(D)S(\lambda)\,dD\,d\lambda}{\int_{\lambda_1}^{\lambda_2}\int_{D_{\min}}^{D_{\max}}\left[\sum_{i=1}^{N} f_i(D)Q_{\text{ext},i}(\lambda, D)A_i(D)\right]N(D)S(\lambda)\,dD\,d\lambda}, \quad \text{and} \tag{2b}$$

$$\langle g\rangle = \frac{\int_{\lambda_1}^{\lambda_2}\int_{D_{\min}}^{D_{\max}}\left[\sum_{i=1}^{N} f_i(D)g_i(\lambda, D)\omega_i(\lambda, D)Q_{\text{ext},i}(\lambda, D)A_i(D)\right]N(D)S(\lambda)\,dD\,d\lambda}{\int_{\lambda_1}^{\lambda_2}\int_{D_{\min}}^{D_{\max}}\left[\sum_{i=1}^{N} f_i(D)\omega_i(\lambda, D)Q_{\text{ext},i}(\lambda, D)A_i(D)\right]N(D)S(\lambda)\,dD\,d\lambda}, \tag{2c}$$

where $\langle Q_{\text{ext}}\rangle$, $\langle \omega\rangle$, and $\langle g\rangle$ are the broadband-averaged extinction efficiency, single-scattering albedo, and asymmetry factor, respectively; λ_1 and λ_2 are wavelength limits of the band; i is the index of mixture habit in ice clouds (for N habits); $S(\lambda)$ is the solar irradiance; and f is the fraction of the habit in the PSD. Note that $\sum_{i=1}^{N} f_i = 1$. At IR wavelengths, $S(\lambda)$ is replaced with the Planck function $B(\lambda)$ at a temperature typical for ice clouds. To represent the thermal IR emission of an ice cloud, an ice cloud temperature of 233 K was used by EB and FU, whereas a temperature of 250 K was used by CH99.

Different ice cloud habit distributions have been used to infer cloud properties from solar and infrared measurements (e.g., Yang et al. 2005; Baum et al. 2005b; King et al. 2004, 2006). For example, the collection 4

TABLE 2. Spectral band schemes for the parameterization of scattering and absorption properties of ice clouds.

Parameterization	Solar spectral band	IR spectral band
EB	0.25–0.7, 0.7–1.3, 1.3–1.9, 1.9–2.5, 2.5–3.5 μm $\tau = \text{IWP}(a_0 + a_1/r_e)$, $1 - \omega = b_0 + b_1 r_e$, $g = c_0 + c_1 r_e$ τ is optical thickness, ω is single-scattering albedo, IWP is ice water path, g is asymmetry factor, and r_e is effective particle radius.	4–8, 8–12.5, 12.5–20, 20–35, 35–200 μm $\kappa = a_0 + a_1/r_e$ κ is mass absorption coefficient.
Fu and Liou (1993), Fu (1996), FU	0.2–0.7, 0.7–1.3, 1.3–1.9, 1.9–2.5, 2.5–3.5, 3.5–4.0 μm $\beta = \text{IWC}(a_0 + a_1/D_{ge})$, $1 - \omega = b_0 + b_1 D_{ge} + b_2 D_{ge}^2 + b_3 D_{ge}^3$, $g = c_0 + c_1 D_{ge} + c_2 D_{ge}^2 + c_3 D_{ge}^3$, $f_\delta = c_0 + c_1 D_{ge} + c_2 D_{ge}^2 + c_3 D_{ge}^3$ β is extinction coefficient, IWC is ice water content, f_δ is δ-function transmission, and D_{ge} is generalized effective size.	2200–1900, 1900–1700, 1700–1400, 1400–1250, 1250–1100, 1100–980, 980–800, 800–670, 670–540, 540–400, 400–280, 280–1 cm^{-1} $\beta = \text{IWC}(a_0 + a_1/D_{ge} + a_2/D_{ge}^2)$, $\beta_a = \text{IWC}(b_0/D_{ge} + b_1 + b_2 D_{ge} + b_3 D_{ge}^2)$, $g = c_0 + c_1 D_{ge} + c_2 D_{ge}^2 + c_3 D_{ge}^3$, $1 - \omega = \beta_a/\beta$ β_a is absorption coefficient.
CH99, CH02	0.175–0.225, 0.225–0.28 (0.225–0.245, 0.26–0.28), 0.245–0.26, 0.28–0.295, 0.295–0.31, 0.31–0.32, 0.32–0.40, 0.40–0.70, 0.70–1.22, 1.22–2.27, 2.27–10.0 μm $\beta = \text{IWC}(a_0 + a_1/r_e)$, $1 - \omega = b_0 + b_1 r_e + b_2 r_e^2$, $g = c_0 + c_1 r_e + c_2 r_e^2$	3000–1900, 1900–1380, 1380–1215, 1215–1100, 1100–980, 980–800, 800–620, 620–540, 540–340, 340–0 cm^{-1} $\beta = \text{IWC}(a_0 + a_1/r_e^{a_2})$, $\omega = b_0 + b_1 r_e + b_2 r_e^2 + b_3 r_e^3$, $g = c_0 + c_1 r_e + c_2 r_e^2 + c_3 r_e^3$

MODIS habit mixture was as follows: for $D_{\max} < 70$ μm, 50% bullet rosettes, 25% hollow columns, and 25% plates; for $D_{\max} \geq 70$ μm, 30% aggregates, 30% bullet rosettes, 20% hollow columns, and 20% plates. The habit distribution described in Baum et al. (2005a) is used in the present study. The habit distribution consists of 100% droxtals when $D_{\max} \leq 60$ μm; 15% bullet rosettes, 50% solid columns, and 35% plates when $60 < D_{\max} \leq 1000$ μm; 45% hollow columns, 45% solid columns, and 10% aggregates when $1000 < D_{\max} \leq 2500$ μm; and 97% bullet rosettes and 3% aggregates when $D_{\max} > 2500$ μm.

b. Parameterization schemes

The spectral bands for the parameterization of SW and LW scattering and absorption properties from EB, FU, and CH99/CH02 are listed in Table 2. These schemes have been extensively used in GCMs (e.g., Kiehl et al. 1998; Lubin et al. 1998; Morcrette and Jakob 2000; Oreopoulos et al. 2004) and are considered in the present study.

The broadband bulk scattering properties are parameterized as functions of the effective particle size (EB; Fu and Liou 1993; Fu 1996; FU; CH99; CH02; Key et al. 2002). As shown in Table 2, the mass extinction coefficient (i.e., κ, τ/IWP, or β/IWC, where τ, IWP, β, and IWC are ice cloud optical thickness, ice water path, extinction coefficient, and ice water content, respectively), mass absorption coefficient, single-scattering albedo ω, asymmetry factor g, and truncation factor f_δ are parameterized as a function of effective particle size. However, the fitting of the parameterizations for each scheme is different for the SW and LW. In this study, a common fitting approach for the scattering and absorption properties is used for each parameterization scheme.

The bulk scattering properties are all parameterized in terms of ice cloud effective particle size, which is defined as (e.g., King et al. 2004; Yang et al. 2005; Baum et al. 2005b)

$$D_e = \frac{3}{2} \frac{\int_{D_{\min}}^{D_{\max}} \left[\sum_{i=1}^{N} f_i(D) V_i(D) \right] N(D)\, dD}{\int_{D_{\min}}^{D_{\max}} \left[\sum_{i=1}^{N} f_i(D) A_i(D) \right] N(D)\, dD}. \quad (3)$$

For the SW, the fitting equations are

$$\beta = \text{IWC} \sum_{n=0}^{2} a_n \left(\frac{1}{D_e} \right)^n, \quad (4a)$$

$$1 - \omega = \sum_{n=0}^{5} b_n D_e^n, \quad (4b)$$

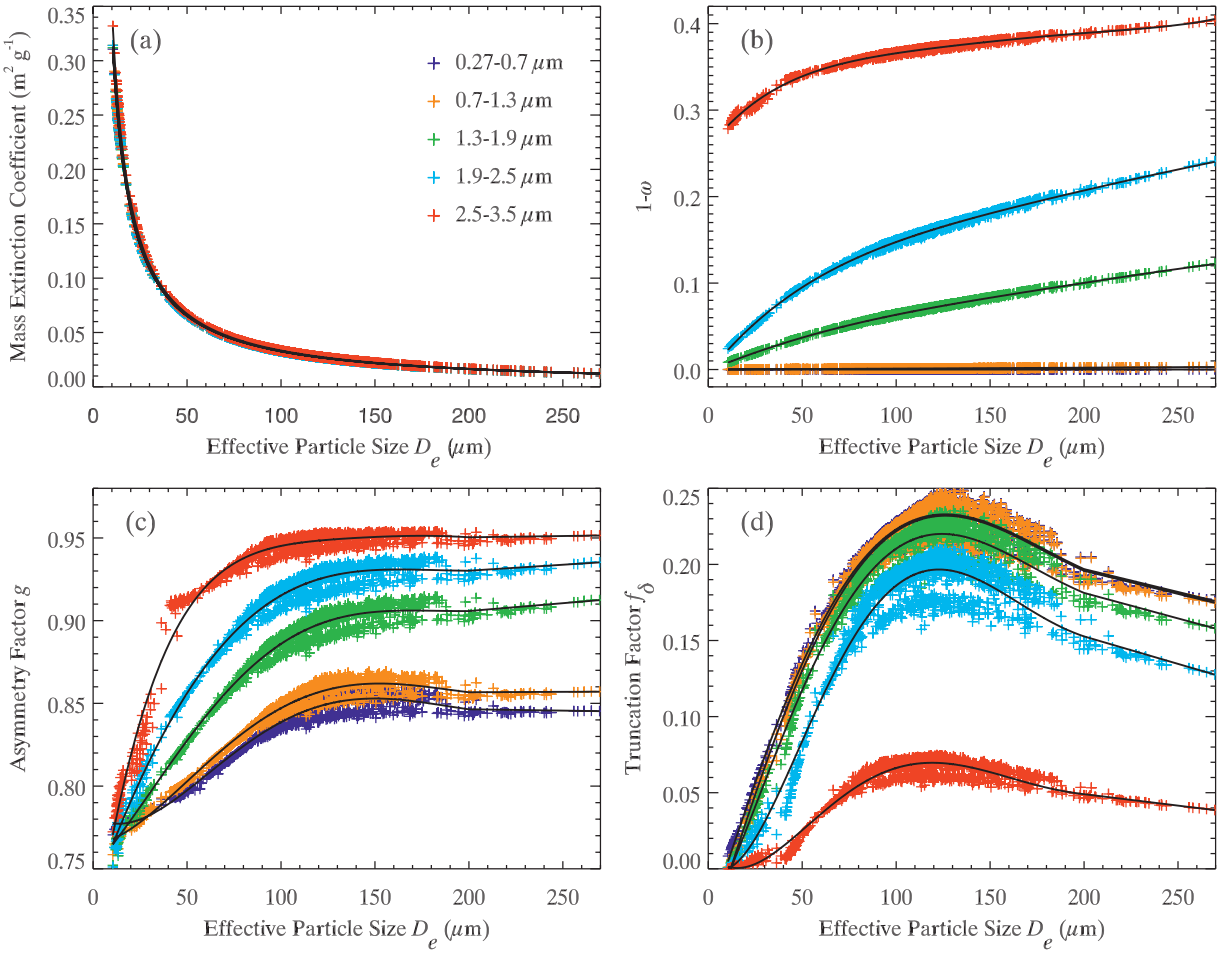

FIG. 2. Parameterizations of mass extinction coefficient β/IWC, single-scattering albedo, asymmetry factor, and truncation factor as a function of effective particle size for solar broad bands used by EB.

$$g = \begin{cases} c_0 + c_1 D_e & \text{for} \quad D_e \le 40\ \mu\text{m} \quad \text{and} \quad D_e \ge 200\ \mu\text{m} \\ \sum_{n=0}^{5} c_n D_e^n & \text{for} \quad 40\ \mu\text{m} < D_e < 200\ \mu\text{m} \end{cases}, \quad \text{and} \tag{4c}$$

$$f_\delta = \begin{cases} \sum_{n=0}^{5} d_n D_e^n & \text{for} \quad D_e < 200\ \mu\text{m} \\ d_0 + d_1 D_e & \text{for} \quad D_e \ge 200\ \mu\text{m} \end{cases}. \tag{4d}$$

For the LW, the fitting equations ($f_\delta = 0$) are given by

$$\beta = \text{IWC} \sum_{n=0}^{5} a_n \left(\frac{1}{D_e}\right)^n, \tag{5a}$$

$$\beta_a = \text{IWC} \sum_{n=0}^{5} b_n \left(\frac{1}{D_e}\right)^n, \quad \text{and} \tag{5b}$$

$$g = \begin{cases} c_0 + c_1 D_e & \text{for} \quad D_e \le 40\ \mu\text{m} \quad \text{and} \quad D_e \ge 200\ \mu\text{m} \\ \sum_{n=0}^{5} c_n D_e^n & \text{for} \quad 40\ \mu\text{m} < D_e < 200\ \mu\text{m} \end{cases}, \tag{5c}$$

where β and β_a are the broadband extinction and absorption coefficients, respectively; IWC is ice water content; D_e is effective particle size; and a, b, c, and d are the fitting coefficients. Appendix, Tables A1–A5 list the values of the fitting coefficients in Eqs. (4a)–(4d) and (5a)–(5c) for different parameterization schemes.

Figure 2 shows the parameterizations of the bulk scattering properties for five SW bands used by EB. The mass extinction coefficient β/IWC, $1 - \omega$, g, and f_δ are plotted as functions of D_e. Each symbol (+) represents a result obtained from one of the 1140 ice cloud PSDs [i.e., Eqs. (2a)–(2c)] and the curves are obtained from the application of Eqs. (4a)–(4d). The sensitivity of the bulk scattering properties to D_e is evident for all bands. For a given D_e, the bulk scattering properties depend on the band, except for β/IWC. The parameterization for the five LW bands used by EB is shown for β/IWC, β_a/IWC, and g in Fig. 3. These bulk scattering properties show sensitivity to D_e, particularly in the case of small D_e.

4. Comparison of SW and LW cloud forcing among the three redeveloped schemes

The parameterizations are used subsequently to investigate the sensitivity of CRF at both the TOA and surface to ice cloud optical thickness and D_e. Furthermore, it is important to understand the differences in CRF that result from the use of the different parameterizations. To isolate the differences of each parameterization (i.e., the bands shown in Table 1) on CRF, a common test bed is first built for computing radiative fluxes at the TOA and surface. The calculation of radiative fluxes is performed by using a combination of the discrete ordinates radiative transfer model (DISORT; Stamnes et al. 1988) and a line-by-line model (LBL; Heidinger 1998) that provides monochromatic molecular absorption in the atmosphere. The standard tropical atmospheric profile in the LBL is used to calculate the transmission for clear sky. CRF here follows the formulas used by, for example, Liou (1992) and Yang et al. (2007):

$$F = F^{\downarrow} - F^{\uparrow} \quad \text{and} \tag{6a}$$

$$\text{CRF} = N(F_{\text{cloud}} - F_{\text{clear}}), \tag{6b}$$

where F is the net total flux (SW plus LW) at the top of the atmosphere or surface; F_{cloud} and F_{clear} are for cloud sky and clear sky, respectively; $\uparrow$ and $\downarrow$ indicate upward and downward fluxes, respectively; and N is cloud fraction.

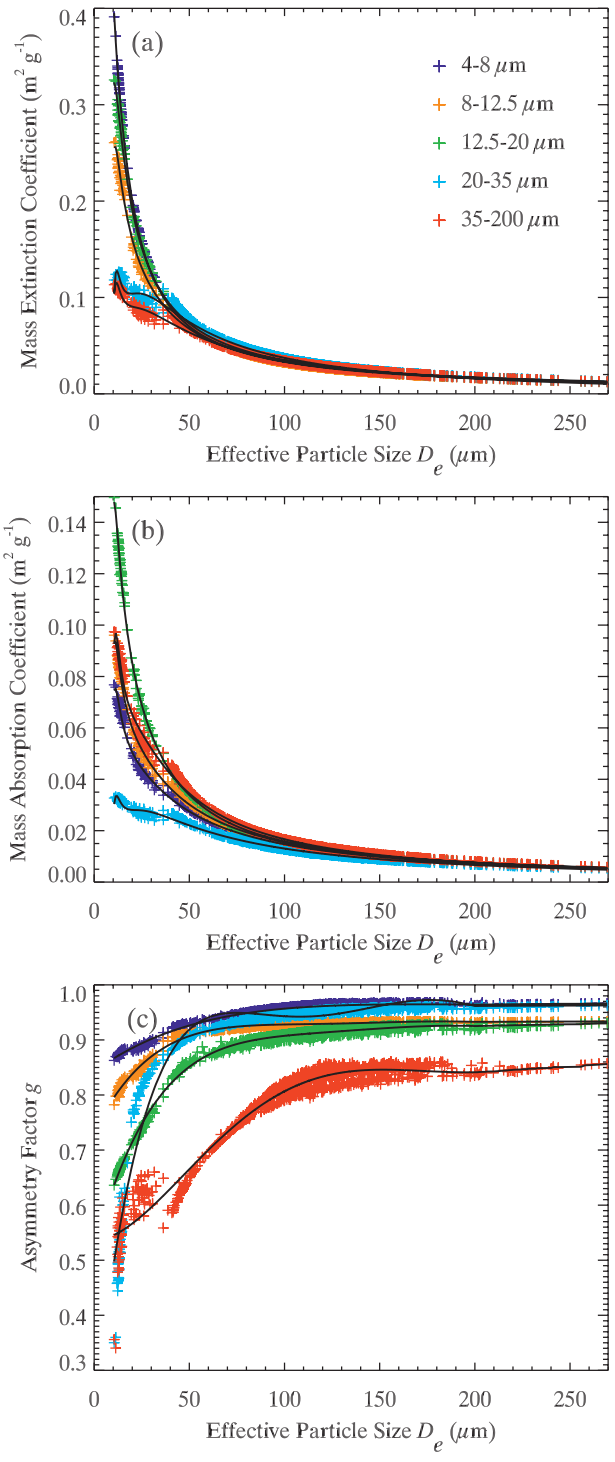

FIG. 3. Parameterizations of mass extinction coefficient, mass absorption coefficient, and asymmetry factor for IR broad bands used by EB.

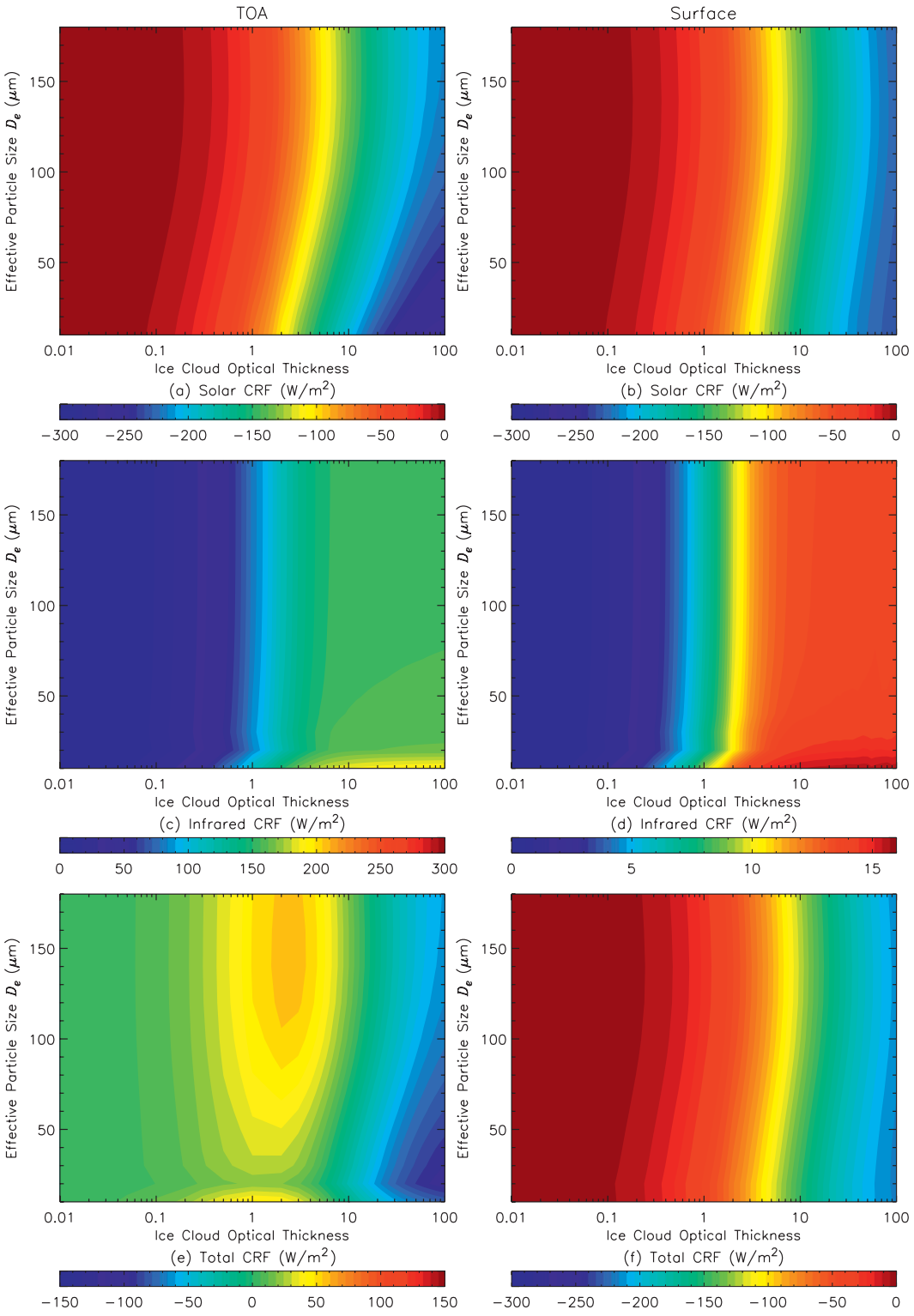

FIG. 4. Variations of CRF (solar, IR, and total) at the (left) TOA and (right) surface as functions of effective particle size and cloud optical thickness. Broadband schemes are from EB. Note that the scales of color bars in all figures are different.

Figure 4 shows the sensitivity of CRF at the TOA and surface to ice cloud optical thickness τ and D_e. The SW, LW, and total radiative forcings are shown separately at both the TOA and surface. The upper boundary of the ice cloud is assumed to be at 12 km, and the cloud layer has a geometrical thickness of 1 km. The solar zenith angle is set at 60°, and the duration of solar illumination is 12 h. The SW and LW radiative forcings are strongly sensitive to τ but weakly sensitive to D_e, particularly for LW radiative forcing. The SW radiative forcing is negative at both the TOA and surface, whereas the LW radiative forcing is positive. The total radiative forcing at the TOA is positive when $\tau < 10$. With increasing τ, the total radiative forcing at the TOA decreases and becomes negative. The total radiative forcing at the surface is negative.

Figure 5 shows the differences of cloud radiative forcing between the FU and EB schemes at the TOA and surface as functions of τ and D_e. The SW radiative forcing at the TOA essentially has no differences. The LW radiative forcing at the TOA has small differences with values in the range of –2 to 2 W m^{-2}. The differences for the total radiative forcing at the TOA have the same features as those for the LW at the TOA. The most distinct differences are shown when $D_e < 50$ μm and $\tau > 0.3$. The SW radiative forcing at the surface has largest differences when $\tau > 3.0$. Most distinct differences for the LW radiative forcing at the surface occur when $D_e < 20$ μm and $1 < \tau < 10$. The same features as the SW radiative forcing at the surface are found for total radiative forcing at the surface.

The differences of CRF between the CH99/CH02 and EB schemes are also investigated (Fig. 6). The differences for radiative forcing at the surface show similar features (Fig. 5), but the differences are larger than those between the FU and EB schemes. The differences for CRF between the CH99/CH02 and EB schemes at the TOA are also larger than those between the FU and EB schemes. However, they have different patterns. The SW and total radiative forcing at the TOA show largest differences when τ is large, whereas the largest differences of LW radiative forcing at the TOA occur when $D_e < 20$ μm and $1 < \tau < 10$. These features generally agree with those shown in the differences of CRF at the surface.

In addition to sizes of ice particles in clouds, the habit mixtures of ice particles vary with temperature, humidity, and vertical wind speed (e.g., Heymsfield and Miloshevich 2003). Test habit mixtures for large ice particles (45% hollow columns, 45% bullet rosettes, and 10% aggregates when $1000 < D_{\max} \leq 2500$ μm; 3% bullet rosettes and 97% aggregates when $D_{\max} > 2500$ μm) are used for the parameterizations for the EB schemes to investigate the sensitivity of ice cloud forcing to habit mixtures. Figure 7 shows cloud radiative forcing differences between the test habits mixtures and those used in MODIS collection 5 (see details of the habit mixture at the end of section 3a). Cloud radiative forcings at both the TOA and the surface have similar features. Small differences are shown for D_e smaller than 20 μm or larger than 150 μm in the cases of SW and total radiative forcings. For LW radiative forcing, differences are only found when $D_e < 20$ μm. Moreover, the radiative forcing differences at the surface are weakly sensitive to habit mixtures with respect to those at the TOA.

5. Differences in LW and SW cloud forcing between the redeveloped and existing schemes

The FU, CH99/CH02, and EB parameterization schemes presented in section 3 are applied to the radiation models developed by Fu and Liou (1993), Chou et al. (1998), and Kiehl et al. (1998), respectively. In this section, ice cloud optical and microphysical properties from the MODIS operational products (collection 5) and atmospheric profiles from AIRS are input into the parameterization of radiative properties of ice particles and atmospheric absorption, respectively, for the radiation models to compute the CRF. Because AIRS and MODIS are both on the National Aeronautics and Space Administration (NASA) Earth Observing System *Aqua* satellite, the products from the two sensors can be collocated in a straightforward manner. Subsequently, the CRF obtained from the MODIS/AIRS products are compared to the CRF differences between the redeveloped and existing parameterization schemes.

Figure 8 shows a MODIS granule over the Indian Ocean at 0820 UTC 21 August 2005. In the false color phase image, the MODIS band 1 reflectance (0.65 μm) is mapped to red, band 7 reflectance (2.1 μm) is mapped to green, and band 31 brightness temperature (11 μm) is mapped to blue, with the scale reversed so that cold clouds have a higher contrast. In this image, water is dark, low-level water clouds are white/yellow, optically thin cirrus is blue, and optically thick ice clouds are blue/magenta. Low-level clouds that have color ranging from yellow to magenta may suggest possible glaciation, because ice particle absorption will act to lower the contribution of the 2.11-μm reflectance in the green channel. Ice clouds are clearly shown by the blue and purple colors. Ice cloud optical thickness and effective radius from the operational MODIS cloud product MYD06 collection 5 are also shown in Fig. 8.

AIRS provides measurements of atmospheric profiles for cloud-free fields of view (FOVs). In the subsequent

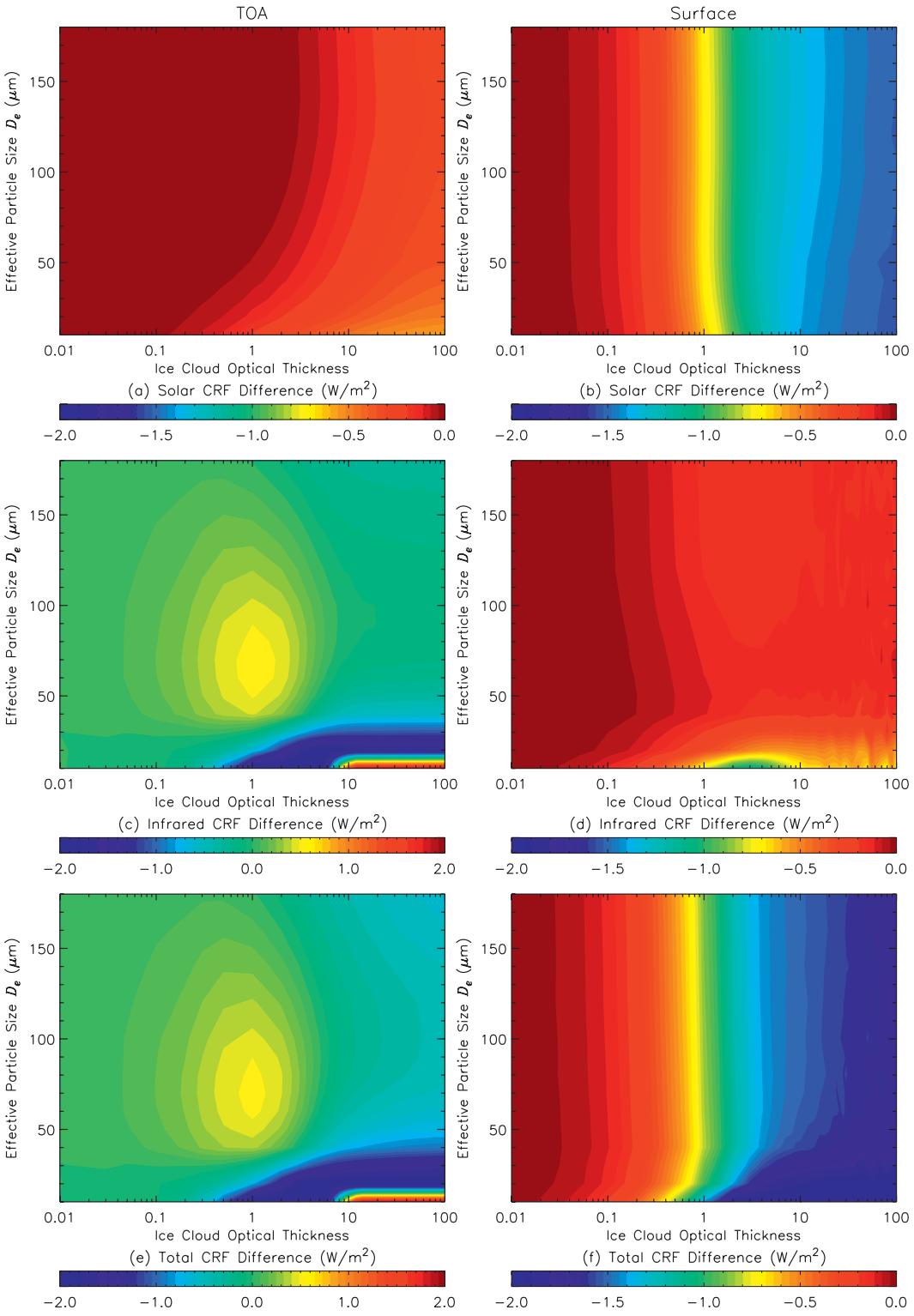

FIG. 5. Differences of CRF (solar, IR, and total) between FU broadband schemes and EB broadband schemes at the (left) TOA and (right) surface as functions of effective particle size and cloud optical thickness.

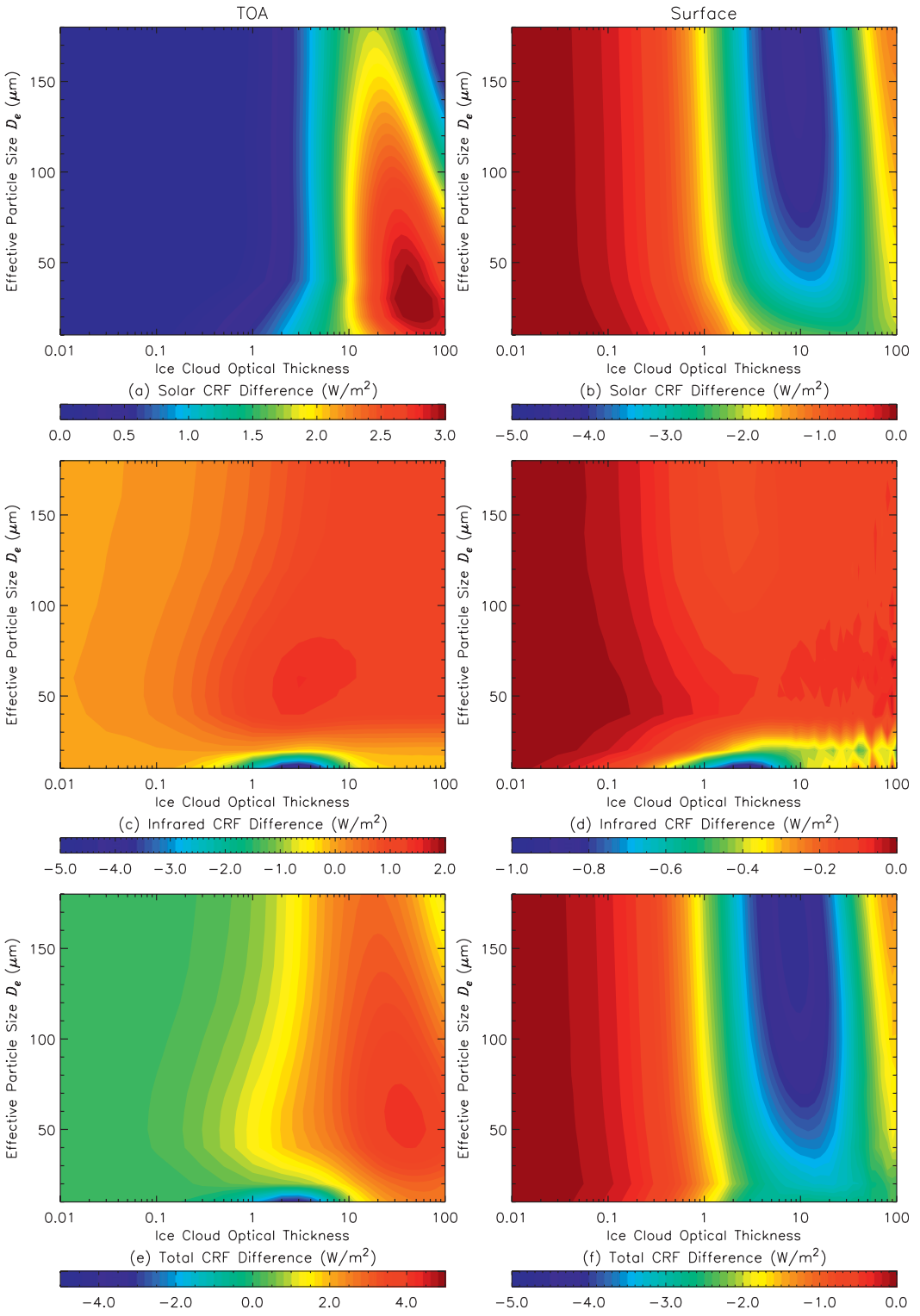

FIG. 6. As in Fig. 5, but for differences of CRF between CH99/CH02 broadband schemes and EB broadband schemes.

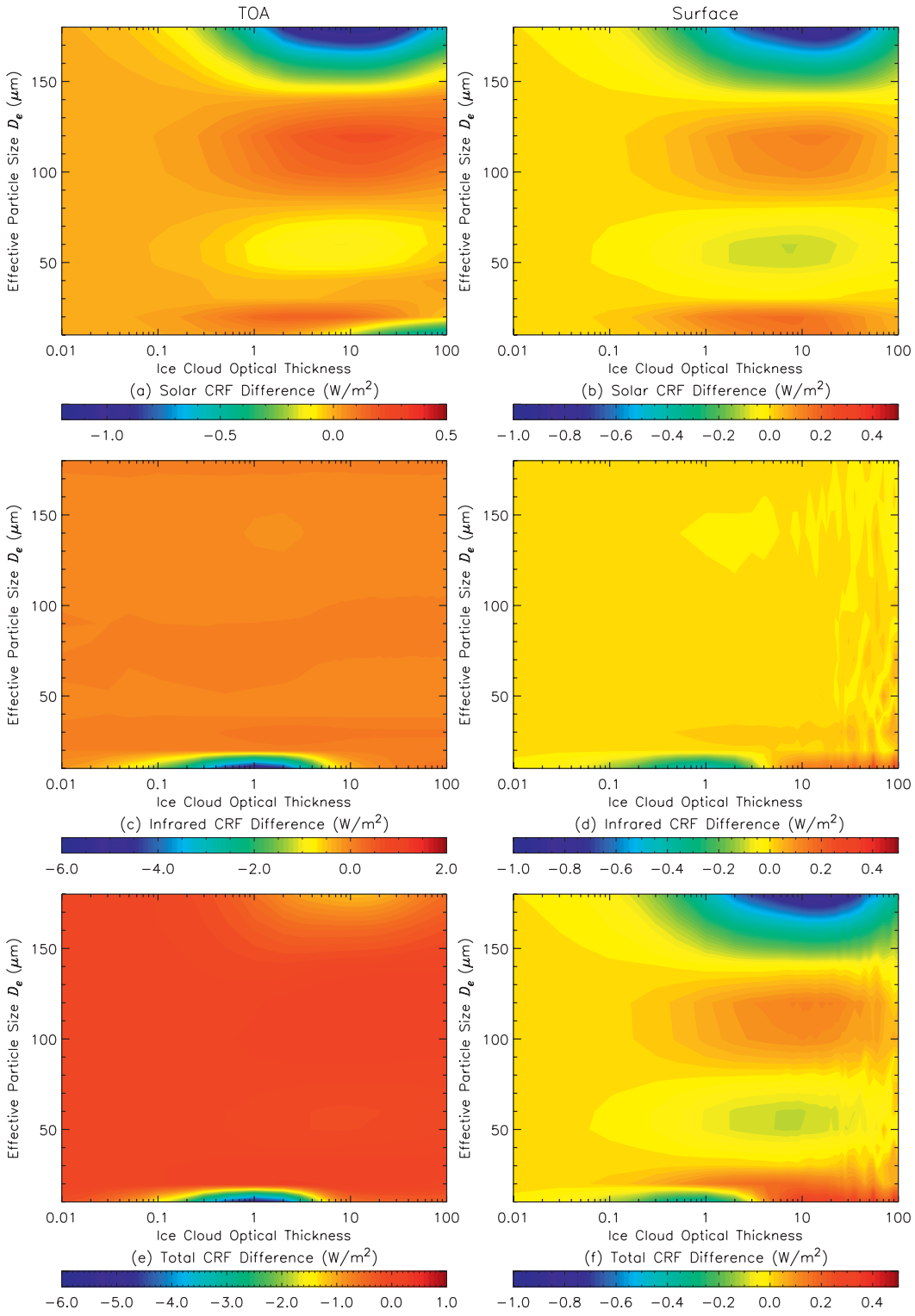

FIG. 7. Differences of CRF between the habit mixtures used by MODIS collection 5 and the test habit mixtures.

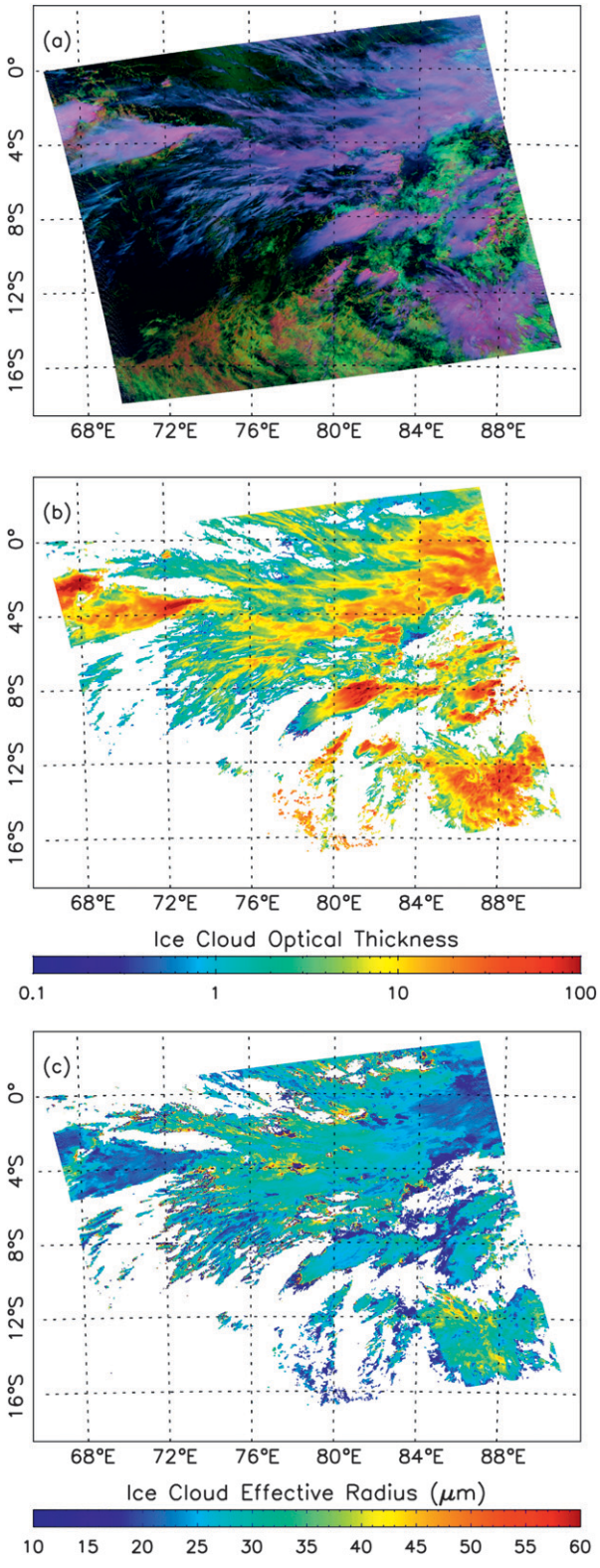

FIG. 8. (a) The false red–green–blue (RGB) image based on three *Aqua* MODIS bands 1, 7, and 31 (gray flipped; see details in context), which was observed over the Indian Ocean at 0820 UTC 21 Aug 2005; (b) ice cloud optical thickness; and (c) ice cloud effective radius.

analysis, two AIRS granules (0817 and 0823 UTC 21 August 2005) are collocated with a MODIS granule. Atmospheric temperature and water vapor profiles are from the AIRS version 5 level 2 standard product (Olsen et al. 2007). The profiles are provided at 28 pressure levels between 0.02 and 1000 hPa. Water vapor is not inferred at pressures less than 50 hPa. The ozone profile is obtained from the standard tropical profile.

Ice cloud–top pressures are provided from the MODIS cloud product MYD06 collection 5 (King et al. 2006). The retrieved ice cloud properties in the granule are assumed to be from a single layer. For the flux calculations, an ice cloud is placed in the layer with pressure level closest to the inferred cloud-top pressure. The ice cloud optical thickness, effective radius, cloud-top height, and the atmospheric profiles are then input into the radiation models to compute the radiative forcing at the TOA and surface.

Figures 9a–d show the SW CRF at the TOA and surface for the CH99/CH02 band model using redeveloped parameterization schemes and the SW CRF differences between the redeveloped and existing parameterization schemes. Although not shown, the SW CRF at the TOA and surface has the same features for both existing and redeveloped parameterization schemes. Their geographical distributions are essentially the same, and the TOA CRF values are similar. The pronounced negative forcing is associated with high values of optical thickness. With the redeveloped parameterization scheme, the SW CRF at the TOA shows weaker negative forcing (Fig. 9c). However, at the surface, the SW CRF calculated from the redeveloped parameterization scheme shows slightly stronger negative forcing relative to the existing scheme (Fig. 9d). The histograms of SW CRF differences at the TOA and surface for the MODIS granule are shown in Figs. 9e,f. The differences at the TOA have a broader distribution than those at the surface. The means of the differences at the TOA and the surface are 15.2 and -5.1 W m^{-2}, with the standard deviation (STDDEV) values of 6.4 and 3.7 W m^{-2}, respectively. The weaker negative TOA forcing and stronger negative surface forcing for the redeveloped CH99/CH02 scheme imply that there is substantially more cloud absorption in the redeveloped scheme. We note that the mean difference in total column absorption is 20 W m^{-2} averaged over the MODIS granule.

The LW CRF obtained from the CH99/CH02 model for the redeveloped parameterization schemes and the differences between the existing and redeveloped parameterization schemes at the TOA and the surface are shown in Figs. 10a–d. All LW CRF have positive values; however, the values at the surface are much smaller than

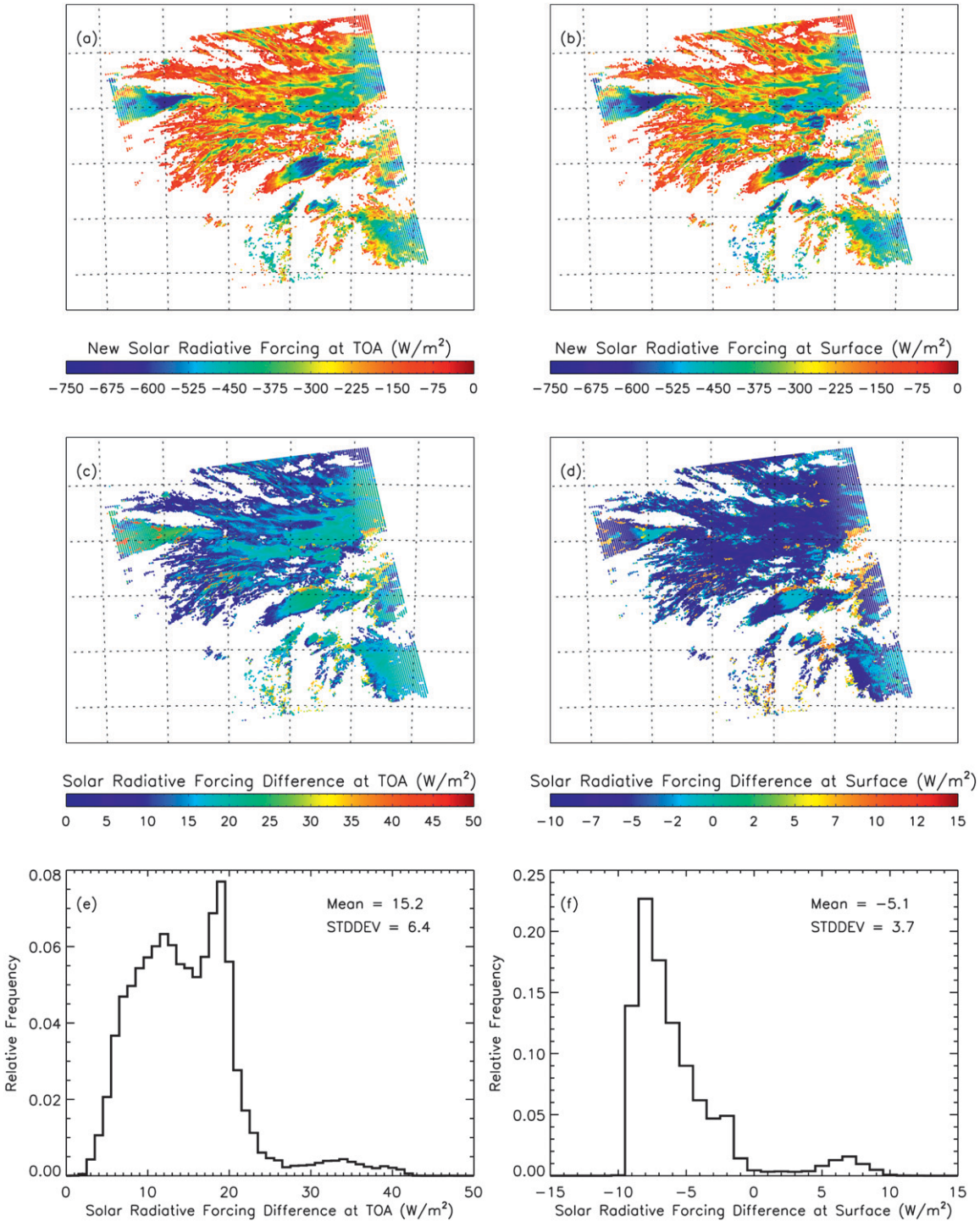

FIG. 9. Solar radiative forcing at the (a) TOA and (b) surface using CH99/CH02 radiative transfer model on the basis of redeveloped parameterization schemes. The differences between redeveloped parameterization schemes and existing ones at the (c) TOA and (d) surface. The histograms of solar radiative forcing differences at the (e) TOA and (f) surface.

those at the TOA. Similar to the SW CRF, the LW CRF for both the existing (figures not shown here) and redeveloped parameterization schemes have essentially the same distributions at both the TOA and surface. Figures 10e,f show the histogram distributions of LW CRF differences at both the TOA and surface between the existing and redeveloped parameterization schemes. The differences at both the TOA and surface have

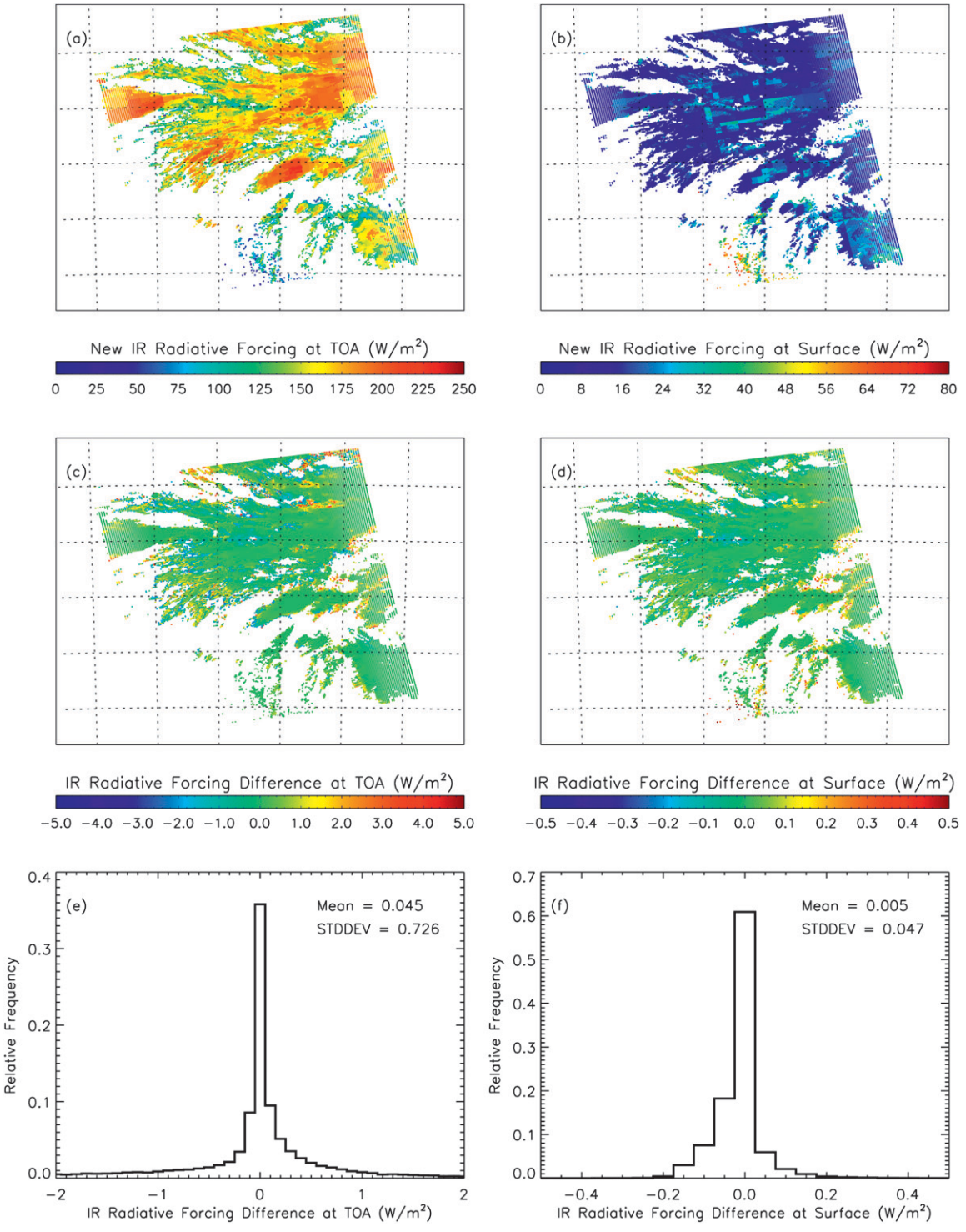

FIG. 10. As in Fig. 9, but for IR radiative forcing differences.

a narrow distribution around 0 W m^{-2}. The means of the differences at the TOA and surface are 0.045 and 0.005 W m^{-2}, with the STDDEV values of 0.726 and 0.047 W m^{-2}, respectively.

Similar to the analysis in Figs. 9 and 10, the SW and LW CRF at the TOA and surface are computed using the existing and redeveloped parameterization schemes for the FU model. The geographical distributions over

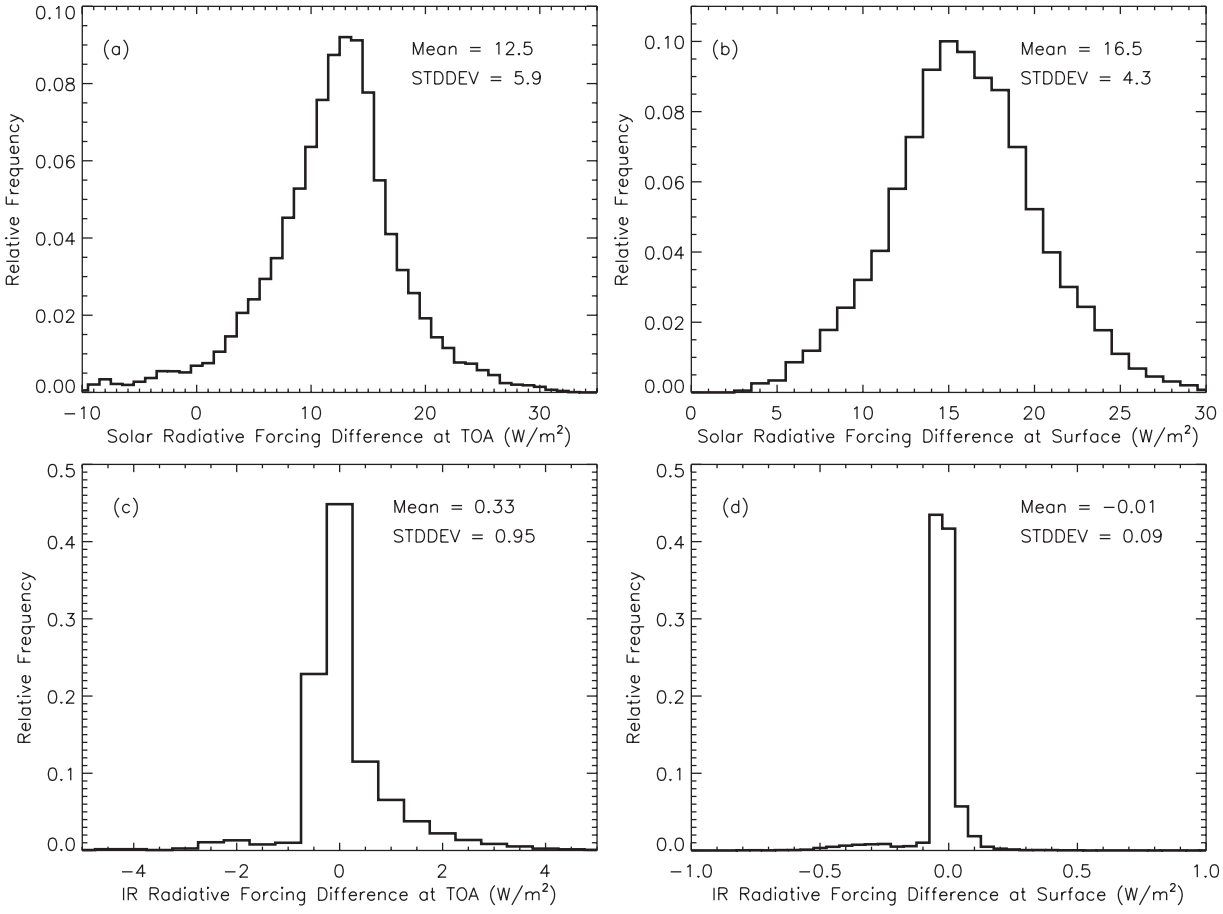

FIG. 11. The histograms of the differences between redeveloped parameterization schemes and existing ones for FU parameterization schemes at the (a) TOA and (b) surface for solar radiative forcing and at the (c) TOA and (d) surface for IR radiative forcing.

the granule have similar features as those of the CH99/CH02 model (figures are not shown here). The histograms of SW and LW CRF differences between the existing and redeveloped parameterization schemes at the TOA and the surface obtained with the FU radiative model are shown in Fig. 11. For the redeveloped parameterization schemes, the SW CRF generally results in a weaker negative forcing at the TOA and surface (Figs. 11a,b). The SW CRF differences at the surface are more pronounced than those at the TOA. The means of the differences at the TOA and surface are 12.5 (STDDEV of 5.9 W m^{-2}) and 16.5 W m^{-2} (STDDEV of 4.3 W m^{-2}), respectively. The LW CRF differences at the TOA (Fig. 11c) are much higher than those at the surface (Fig. 11d). At the TOA, the results obtained on the basis of the redeveloped parameterization are slightly larger than those obtained from the existing parameterization. The means of the LW CRF differences at the TOA and the surface are 0.33 (STDDEV of 0.95 W m^{-2}) and 0.01 W m^{-2} (STDDEV of 0.09 W m^{-2}), respectively. Although the mean value of the LW CRF differences at the TOA is small, the pronounced differences are up to ± 5 W m^{-2} over broad areas (granule not shown here).

The Column Radiation Model (CRM) that is the radiation model used in the National Center for Atmospheric Research (NCAR) Community Climate Model (Kiehl et al. 1998) has been implemented with the EB parameterization schemes. The SW and LW CRF differences using the CRM with both the existing and redeveloped EB parameterization schemes at the TOA and surface are shown in Fig. 12. The geographical distributions of the CRF associated with the existing and redeveloped parameterizations have similar features and are similar to those from the CH99/CH02 and FU radiative models (figures not shown here). The SW CRF differences at the TOA have similar geographical distributions and values as those at the surface (figures not shown here). Both of their histogram distributions are centered near 0 W m^{-2}, with a second broad peak around 5–11 W m^{-2} and a mean value of 0.47 W m^{-2} (STDDEV of 2.0 W m^{-2}).

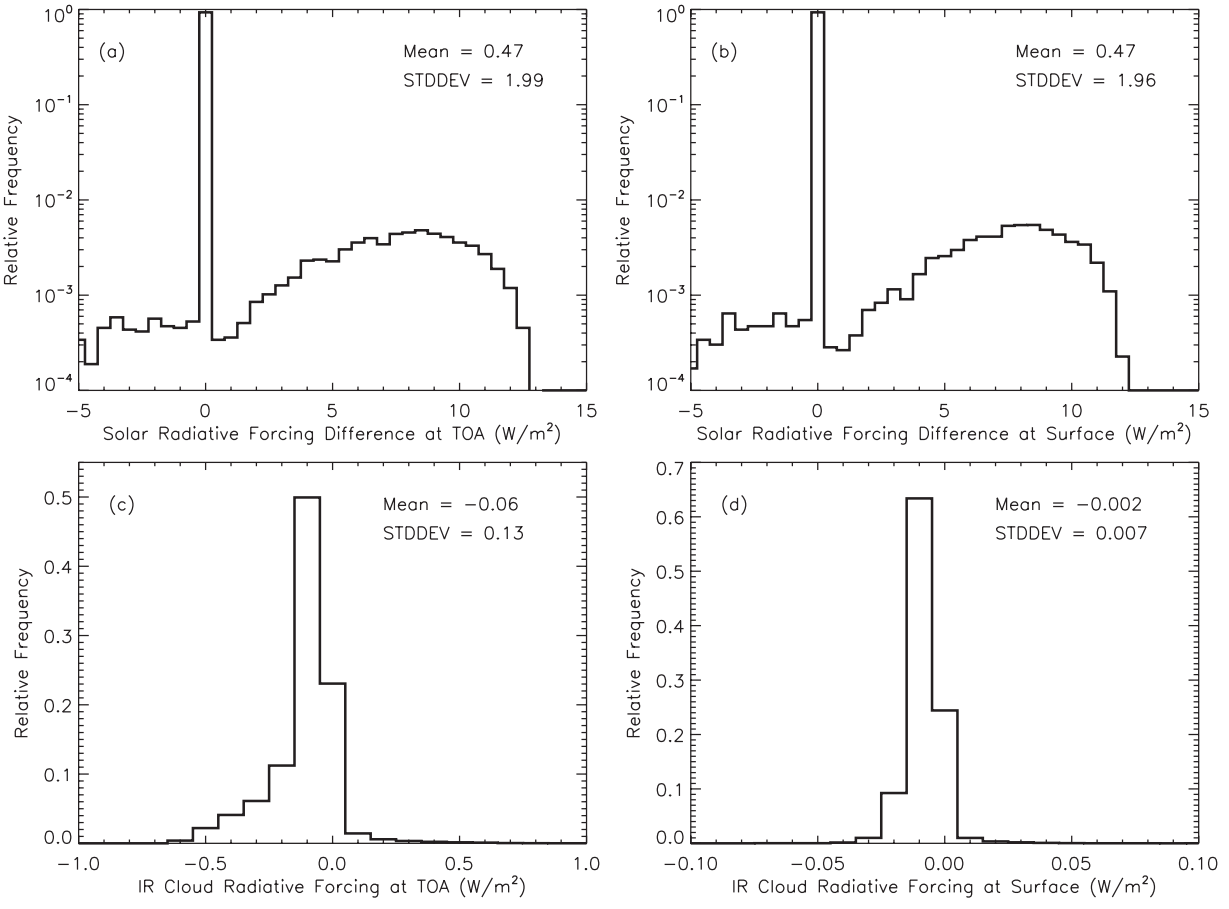

FIG. 12. As in Fig. 11, but for EB radiative parameterization schemes. Note that a logarithm scale is used for the *y* axis for solar radiative forcing.

The parameterization scheme used for the LW in the CRM only takes into account the mass absorption coefficient. The CRM uses a diffusivity factor of 1.66 (e.g., Liou 1992; EB) to calculate diffuse transmission for LW radiation. A similar approach is adopted for the LW CRF for our redeveloped parameterization scheme in this study. There is little difference between the LW CRF of the existing and redeveloped parameterization schemes (Figs. 12c,d). The mean values of the LW CRF differences can be neglected.

6. Conclusions

The ice cloud microphysical and single-scattering properties (developed by, e.g., Yang et al. 2000, 2005; Baum et al. 2005a) have been used to improve retrievals of ice cloud optical and microphysical properties (e.g., Platnick et al. 2003; Baum et al. 2005b, 2007; King et al. 2006). These data can be used for the parameterization of ice cloud radiative properties implemented in climate models to improve climate predictions. In this study, these data are used to redevelop the parameterizations for shortwave (SW) and longwave (LW) radiative properties of ice clouds. The particle size distributions (PSDs) are derived from in situ measurements obtained from five field campaigns in both tropical and midlatitude regions. These PSDs are used to derive the broadband-averaged bulk scattering properties. The ice cloud habit mixtures derived by Baum et al. (2005a), which are for current ice cloud retrievals from the MODIS data (King et al. 2006), are used for the averaging.

The single-scattering properties of ice particles from 0.2 to 100 μm have been computed by Yang et al. (2000, 2005) from a composite method that is based on a combination of the finite-difference time domain technique and an improved geometrical-optics method. Six nonspherical ice crystal habits are considered, including hexagonal solid and hollow columns, hexagonal plates, bullet rosettes, aggregates, and droxtals.

Three parameterization schemes for both SW and LW radiation are considered here: EB, FU, and CH99/CH02; they are listed in Table 2. For these parameterization

TABLE A1. Values of coefficients in Eqs. (4a) and (5a) for the parameterization of mass extinction coefficient β/IWC ($m^2\ g^{-1}$) for solar and IR spectral bands.

Parameterization							
		Coef					
Scheme	Wavelength (μm) or wavenumber (cm^{-1})	Order 0	Order 1	Order 2	Order 3	Order 4	Order 5
Solar radiation (EB)	0.25–0.7	-4.85012×10^{-5}	3.28130	-2.76091×10^{-1}	—	—	—
	0.7–1.3	3.04876×10^{-5}	3.27349	1.19864×10^{-1}	—	—	—
	1.3–1.9	1.10864×10^{-5}	3.26815	2.73869×10^{-1}	—	—	—
	1.9–2.5	2.29914×10^{-4}	3.23372	1.08904	—	—	—
	2.5–3.5	8.06552×10^{-5}	3.29801	2.72244	—	—	—
IR radiation (EB)	4–8	-1.02161×10^{-3}	3.68154	-4.20165×10^{1}	2.42899×10^{3}	-4.22788×10^{4}	2.39289×10^{5}
	8–12.5	1.70180×10^{-3}	2.81532	3.20298×10^{1}	6.83797×10^{1}	-1.99284×10^{4}	1.80772×10^{5}
	12.5–20	1.49416×10^{-4}	3.38893	-1.12308×10^{1}	2.32169×10^{3}	-5.89355×10^{4}	4.04523×10^{5}
	20–35	1.91492×10^{-3}	2.47608	1.34027×10^{2}	-3.69086×10^{3}	1.51049×10^{4}	1.19439×10^{5}
	35–200	2.94384×10^{-3}	2.42664	1.10890×10^{2}	-4.90740×10^{3}	6.25567×10^{4}	-2.54200×10^{5}
Solar radiation (Fu and Liou 1993; Fu 1996)	0.2–0.7	-4.81358×10^{-5}	3.28125	-2.73251×10^{-1}	—	—	—
	0.7–1.3	3.04876×10^{-5}	3.27349	1.19864×10^{-1}	—	—	—
	1.3–1.9	1.10864×10^{-5}	3.26815	2.73869×10^{-1}	—	—	—
	1.9–2.5	2.29914×10^{-4}	3.23372	1.08904	—	—	—
	2.5–3.5	8.06552×10^{-5}	3.29801	2.72244	—	—	—
	3.5–4.0	3.67309×10^{-4}	3.26680	8.43629	—	—	—
IR radiation (Fu and Liou 1993; FU)	2200–1900	-5.84374×10^{-4}	3.48974	−7.81567	4.38675×10^{2}	-2.17246×10^{3}	-1.69303×10^{4}
	1900–1700	-1.95060×10^{-3}	3.98626	-7.67961×10^{1}	3.93746×10^{3}	-6.81663×10^{4}	3.89499×10^{5}
	1700–1400	-1.66910×10^{-3}	3.92764	-7.59167×10^{1}	4.14634×10^{3}	-7.55400×10^{4}	4.46144×10^{5}
	1400–1250	-9.79255×10^{-4}	3.77038	-6.93484×10^{1}	4.34294×10^{3}	-8.40730×10^{4}	5.12429×10^{5}
	1250–1100	1.98591×10^{-3}	2.88966	5.82188	1.90844×10^{3}	-5.24626×10^{4}	3.63108×10^{5}
	1100–980	2.50551×10^{-3}	2.39098	9.16350×10^{1}	-2.36909×10^{3}	1.67413×10^{4}	-1.32028×10^{4}
	980–800	6.21685×10^{-4}	3.08573	1.51155×10^{1}	-2.66819×10^{2}	-8.39858×10^{3}	1.06090×10^{5}
	800–670	-4.60768×10^{-4}	3.56645	-2.93068×10^{1}	2.59761×10^{3}	-5.69007×10^{4}	3.69406×10^{5}
	670–540	6.47256×10^{-4}	3.26671	1.02595	2.20465×10^{3}	-6.15603×10^{4}	4.33629×10^{5}
	540–400	1.78399×10^{-3}	2.53657	1.03378×10^{2}	-1.17674×10^{3}	-3.06181×10^{4}	3.74117×10^{5}
	400–280	2.05724×10^{-3}	2.61808	1.32600×10^{2}	-5.54721×10^{3}	5.97021×10^{4}	-1.67647×10^{5}
	280–1	3.03358×10^{-3}	2.39861	1.15003×10^{2}	-4.95589×10^{3}	6.20272×10^{4}	-2.46229×10^{5}
Solar radiation (Chou and Suarez 2002)	0.175–0.225	1.73345×10^{-5}	3.27754	-1.65665×10^{-1}	—	—	—
	0.225–0.28	3.36117×10^{-5}	3.27219	-1.22836×10^{-2}	—	—	—
	0.245–0.26	5.63177×10^{-5}	3.26840	1.00787×10^{-1}	—	—	—
	0.28–0.295	4.04939×10^{-5}	3.27083	-3.59439×10^{-2}	—	—	—
	0.295–0.31	6.62315×10^{-5}	3.26828	-2.34926×10^{-2}	—	—	—
	0.31–0.32	5.15135×10^{-5}	3.26839	6.43369×10^{-2}	—	—	—
	0.32–0.40	4.11749×10^{-5}	3.26658	4.55623×10^{-2}	—	—	—
	0.40–0.70	-6.79094×10^{-5}	3.28429	-3.43970×10^{-1}	—	—	—
	0.70–1.22	3.53295×10^{-5}	3.27321	1.40381×10^{-1}	—	—	—
	1.22–2.27	4.37031×10^{-5}	3.26417	2.65461×10^{-1}	—	—	—
	2.27–10.0	4.66242×10^{-5}	3.27790	4.15521	—	—	—
IR radiation (CH02)	3000–1900	-4.46656×10^{-4}	3.46060	-1.01845×10^{1}	7.25593×10^{2}	-9.80669×10^{3}	4.04259×10^{4}
	1900–1380	-1.78937×10^{-3}	3.95327	-7.64172×10^{1}	4.06579×10^{3}	-7.25581×10^{4}	4.22949×10^{5}
	1380–1215	-6.04469×10^{-4}	3.66835	-6.18883×10^{1}	4.16701×10^{3}	-8.26764×10^{4}	5.09799×10^{5}
	1215–1100	2.47416×10^{-3}	2.73307	2.06572×10^{1}	1.35476×10^{3}	-4.43176×10^{4}	3.20380×10^{5}
	1100–980	2.50539×10^{-3}	2.39092	9.16538×10^{1}	-2.36997×10^{3}	1.67511×10^{4}	-1.32288×10^{4}
	980–800	6.21072×10^{-4}	3.08602	1.50815×10^{1}	-2.64926×10^{2}	-8.42686×10^{3}	1.06226×10^{5}
	800–620	-3.33392×10^{-4}	3.53531	-2.59801×10^{1}	2.59263×10^{3}	-5.82356×10^{4}	3.81074×10^{5}
	620–540	1.07357×10^{-3}	3.14061	1.32148×10^{1}	1.92342×10^{3}	-6.07693×10^{4}	4.44498×10^{5}
	540–340	1.62619×10^{-3}	2.59717	1.10306×10^{2}	-1.97169×10^{3}	-1.61087×10^{4}	2.95925×10^{5}
	340–0	3.23067×10^{-3}	2.36978	1.21070×10^{2}	-5.63912×10^{3}	7.52124×10^{4}	-3.22149×10^{5}

TABLE A2. Values of coefficients in Eqs. (4b) and (5b) for the parameterization of single-scattering albedo (1-ω) for solar spectral bands and mass absorption coefficient β_a/IWC ($m^2\ g^{-1}$) for IR spectral bands.

		Parameterization					
		Coef					
Scheme	Wavelength (μm) or wavenumber (cm^{-1})	Order 0	Order 1	Order 2	Order 3	Order 4	Order 5
Solar radiation (EB)	0.25–0.7	-3.60704×10^{-7}	7.21850×10^{-8}	7.94411×10^{-11}	3.75466×10^{-13}	-3.93269×10^{-15}	7.68815×10^{-18}
	0.7–1.3	-1.79060×10^{-5}	1.18571×10^{-5}	-1.72893×10^{-9}	-1.25842×10^{-10}	8.65099×10^{-13}	-1.55388×10^{-15}
	1.3–1.9	-3.92591×10^{-3}	1.02397×10^{-3}	-4.99331×10^{-6}	1.74700×10^{-8}	-2.83075×10^{-11}	1.42681×10^{-14}
	1.9–2.5	-1.00176×10^{-2}	3.00763×10^{-3}	-2.33310×10^{-5}	1.18262×10^{-7}	-3.19406×10^{-10}	3.55567×10^{-13}
	2.5–3.5	2.57520×10^{-1}	2.74169×10^{-3}	-3.01662×10^{-5}	1.87106×10^{-7}	-5.88805×10^{-10}	7.34490×10^{-13}
IR radiation (EB)	4–8	6.49929×10^{-4}	1.31328	1.44874×10^{1}	-7.19709×10^{2}	7.18717×10^{3}	-1.54992×10^{4}
	8–12.5	9.29973×10^{-4}	1.24956	2.85449×10^{1}	-9.88834×10^{2}	8.92379×10^{3}	-1.59637×10^{4}
	12.5–20	8.24728×10^{-4}	1.26901	2.04267×10^{1}	3.25229×10^{2}	-1.91284×10^{4}	1.60487×10^{5}
	20–35	1.35264×10^{-3}	1.00092	3.42079×10^{1}	-2.22935×10^{3}	3.77982×10^{4}	-2.07991×10^{5}
	35–200	2.22135×10^{-3}	7.85650×10^{-1}	8.71563×10^{1}	-2.61593×10^{3}	2.56384×10^{4}	-7.15300×10^{4}
Solar radiation (Fu and Liou 1993; Fu 1996)	0.2–0.7	6.43115×10^{-7}	2.17070×10^{-8}	9.77892×10^{-10}	-6.21738×10^{-12}	1.76521×10^{-14}	-1.81261×10^{-17}
	0.7–1.3	-1.79060×10^{-5}	1.18571×10^{-5}	-1.72893×10^{-9}	-1.25842×10^{-10}	8.65099×10^{-13}	-1.55388×10^{-15}
	1.3–1.9	-3.92591×10^{-3}	1.02397×10^{-3}	-4.99331×10^{-6}	1.74700×10^{-8}	-2.83075×10^{-11}	1.42681×10^{-14}
	1.9–2.5	-1.00176×10^{-2}	3.00763×10^{-3}	-2.33310×10^{-5}	1.18262×10^{-7}	-3.19406×10^{-10}	3.55567×10^{-13}
	2.5–3.5	2.57520×10^{-1}	2.74169×10^{-3}	-3.01662×10^{-5}	1.87106×10^{-7}	-5.88805×10^{-10}	7.34490×10^{-13}
	3.5–4.0	5.93267×10^{-2}	1.03567×10^{-2}	-1.33544×10^{-4}	8.79558×10^{-7}	-2.84586×10^{-9}	3.57453×10^{-12}
IR radiation (Fu and Liou 1993; FU)	2200–1900	6.24226×10^{-4}	1.29894	1.13256×10^{1}	-9.66906×10^{2}	1.46968×10^{4}	-6.99588×10^{4}
	1900–1700	7.73617×10^{-4}	1.27757	2.13243×10^{1}	-1.03345×10^{3}	1.21481×10^{4}	-4.19730×10^{4}
	1700–1400	5.81127×10^{-4}	1.38228	1.35590×10^{1}	6.16497×10^{1}	-1.19034×10^{4}	1.13310×10^{5}
	1400–1250	9.49216×10^{-4}	1.25454	2.74192×10^{1}	-6.74666×10^{2}	3.75930×10^{2}	4.57448×10^{4}
	1250–1100	1.23227×10^{-3}	1.15138	3.68333×10^{1}	-1.42095×10^{3}	1.50424×10^{4}	-4.38139×10^{4}
	1100–980	1.21855×10^{-3}	1.15289	4.21575×10^{1}	-1.86552×10^{3}	2.46301×10^{4}	-1.06753×10^{5}
	980–800	2.74461×10^{-4}	1.46504	5.60159	3.53007×10^{2}	-1.29488×10^{4}	1.00429×10^{5}
	800–670	1.67580×10^{-4}	1.48434	−4.22907	1.50078×10^{3}	-3.66616×10^{4}	2.47934×10^{5}
	670–540	1.38424×10^{-3}	1.09490	4.03082×10^{1}	-5.18670×10^{2}	-8.38682×10^{3}	1.16274×10^{5}
	540–400	1.89969×10^{-3}	8.34491×10^{-1}	5.59322×10^{1}	-2.66596×10^{3}	4.00202×10^{4}	-2.01957×10^{5}
	400–280	9.72994×10^{-4}	1.14224	2.59433×10^{1}	-2.03652×10^{3}	3.59358×10^{4}	-2.02009×10^{5}
	280–1	2.28944×10^{-3}	7.60656×10^{-1}	8.98854×10^{1}	-2.64204×10^{3}	2.52381×10^{4}	-6.63449×10^{4}
Solar radiation (Chou and Suarez 2002)	0.175–0.225	-3.43409×10^{-6}	1.04906×10^{-6}	-2.60706×10^{-9}	8.68706×10^{-12}	9.13576×10^{-15}	-5.46986×10^{-17}
	0.225–0.28	-1.36014×10^{-6}	4.83944×10^{-7}	-8.59651×10^{-10}	1.79798×10^{-12}	9.27644×10^{-15}	-2.74081×10^{-17}
	0.245–0.26	-8.76689×10^{-7}	4.70625×10^{-7}	-1.82964×10^{-9}	1.28657×10^{-11}	-4.01959×10^{-14}	4.85971×10^{-17}
	0.28–0.295	-7.86574×10^{-7}	3.08124×10^{-7}	5.55414×10^{-11}	-4.77727×10^{-12}	3.02819×10^{-14}	-5.31798×10^{-17}
	0.295–0.31	-1.58205×10^{-6}	3.33687×10^{-7}	-1.31488×10^{-9}	6.51993×10^{-12}	-1.01819×10^{-14}	-4.47501×10^{-19}
	0.31–0.32	-3.94555×10^{-6}	4.67314×10^{-7}	-4.87984×10^{-9}	3.71176×10^{-11}	-1.26337×10^{-13}	1.60285×10^{-16}
	0.32–0.40	-2.67018×10^{-6}	1.86684×10^{-7}	-7.83596×10^{-10}	2.12648×10^{-12}	3.04922×10^{-15}	-1.49719×10^{-17}
	0.40–0.70	1.23312×10^{-6}	-2.05394×10^{-8}	1.42655×10^{-9}	-9.90186×10^{-12}	3.31953×10^{-14}	-4.33846×10^{-17}
	0.70–1.22	-1.22070×10^{-5}	7.35883×10^{-6}	-1.58149×10^{-9}	-7.24528×10^{-11}	5.23448×10^{-13}	-9.55553×10^{-16}
	1.22–2.27	-4.45879×10^{-3}	1.27945×10^{-3}	-8.06034×10^{-6}	3.58130×10^{-8}	-8.41253×10^{-11}	8.18117×10^{-14}
	2.27–10.0	1.59255×10^{-1}	4.49849×10^{-3}	-5.48103×10^{-5}	3.60091×10^{-7}	-1.17072×10^{-9}	1.48151×10^{-12}
IR radiation (CH02)	3000–1900	5.55561×10^{-4}	1.30111	1.16802×10^{1}	-9.65127×10^{2}	1.55583×10^{4}	-7.98957×10^{4}
	1900–1380	6.73891×10^{-4}	1.33337	1.73177×10^{1}	-4.36650×10^{2}	-1.05543×10^{3}	4.35499×10^{4}
	1380–1215	9.97470×10^{-4}	1.23831	2.85048×10^{1}	-7.64655×10^{2}	2.06694×10^{3}	3.58703×10^{4}
	1215–1100	1.26727×10^{-3}	1.13738	3.87111×10^{1}	-1.55374×10^{3}	1.76857×10^{4}	-6.03088×10^{4}
	1100–980	1.21843×10^{-3}	1.15293	4.21545×10^{1}	-1.86543×10^{3}	2.46289×10^{4}	-1.06748×10^{5}
	980–800	2.74239×10^{-4}	1.46508	5.59011	3.54010×10^{2}	-1.29662×10^{4}	1.00525×10^{5}
	800–620	3.28330×10^{-4}	1.43587	1.31145	1.27899×10^{3}	-3.42639×10^{4}	2.40667×10^{5}
	620–540	1.78488×10^{-3}	9.56961×10^{-1}	5.60913×10^{1}	-1.32992×10^{3}	5.27148×10^{3}	4.00035×10^{4}
	540–340	1.66728×10^{-3}	9.04004×10^{-1}	4.70192×10^{1}	-2.46868×10^{3}	3.86671×10^{4}	-2.01523×10^{5}
	340–0	1.80112×10^{-3}	9.20311×10^{-1}	6.86144×10^{1}	-2.55427×10^{3}	3.14138×10^{4}	-1.28232×10^{5}

TABLE A3. Values of coefficients in Eqs. (4c) and (5c) for the parameterization of asymmetry factor g for solar and IR spectral bands when effective particle sizes are between 40 and 200 μm.

		Parameterization					
		Coef					
Scheme	Wavelength (μm) or wavenumber (cm^{-1})	Order 0	Order 1	Order 2	Order 3	Order 4	Order 5
Solar radiation (EB)	0.25–0.7	8.07497×10^{-1}	-1.92598×10^{-3}	5.24357×10^{-5}	-4.26916×10^{-7}	1.43684×10^{-9}	-1.74088×10^{-12}
	0.7–1.3	7.75943×10^{-1}	-4.49352×10^{-4}	3.14267×10^{-5}	-2.83986×10^{-7}	9.74800×10^{-10}	-1.16964×10^{-12}
	1.3–1.9	7.46554×10^{-1}	1.35717×10^{-3}	1.25859×10^{-5}	-1.87230×10^{-7}	7.47012×10^{-10}	-9.78142×10^{-13}
	1.9–2.5	7.30718×10^{-1}	3.20195×10^{-3}	-1.38091×10^{-5}	-1.72949×10^{-8}	2.32790×10^{-10}	-3.83473×10^{-13}
	2.5–3.5	7.52409×10^{-1}	5.62919×10^{-3}	-6.75758×10^{-5}	4.21108×10^{-7}	-1.32903×10^{-9}	1.66305×10^{-12}
IR radiation (EB)	4–8	8.31645×10^{-1}	3.07420×10^{-3}	-3.09908×10^{-5}	1.73024×10^{-7}	-5.22630×10^{-10}	6.54418×10^{-13}
	8–12.5	7.75708×10^{-1}	5.17535×10^{-3}	-7.06035×10^{-5}	4.77777×10^{-7}	-1.57197×10^{-9}	1.99623×10^{-12}
	12.5–20	6.11260×10^{-1}	8.60728×10^{-3}	-1.03050×10^{-4}	6.40516×10^{-7}	-1.99731×10^{-9}	2.45407×10^{-12}
	20–35	5.17094×10^{-1}	1.51784×10^{-2}	-2.13950×10^{-4}	1.48134×10^{-6}	-4.94504×10^{-9}	6.33447×10^{-12}
	35–200	1.92909×10^{-1}	1.33937×10^{-2}	-1.05847×10^{-4}	4.06454×10^{-7}	-7.82145×10^{-10}	6.44581×10^{-13}
Solar radiation (Fu and Liou 1993; Fu 1996)	0.2–0.7	8.07511×10^{-1}	-1.92664×10^{-3}	5.24441×10^{-5}	-4.26965×10^{-7}	1.43698×10^{-9}	-1.74104×10^{-12}
	0.7–1.3	7.75943×10^{-1}	-4.49352×10^{-4}	3.14267×10^{-5}	-2.83986×10^{-7}	9.74800×10^{-10}	-1.16964×10^{-12}
	1.3–1.9	7.46554×10^{-1}	1.35717×10^{-3}	1.25859×10^{-5}	-1.87230×10^{-7}	7.47012×10^{-10}	-9.78142×10^{-13}
	1.9–2.5	7.30718×10^{-1}	3.20195×10^{-3}	-1.38091×10^{-5}	-1.72949×10^{-8}	2.32790×10^{-10}	-3.83473×10^{-13}
	2.5–3.5	7.52409×10^{-1}	5.62919×10^{-3}	-6.75758×10^{-5}	4.21108×10^{-7}	-1.32903×10^{-9}	1.66305×10^{-12}
	3.5–4.0	7.83219×10^{-1}	1.82971×10^{-3}	7.50923×10^{-6}	-1.71007×10^{-7}	7.48606×10^{-10}	-1.03508×10^{-12}
IR radiation (Fu and Liou 1993; FU)	2200–1900	8.40126×10^{-1}	5.59038×10^{-4}	1.79784×10^{-5}	-1.99315×10^{-7}	7.29916×10^{-10}	-9.03526×10^{-13}
	1900–1700	8.53661×10^{-1}	3.14643×10^{-3}	-3.64004×10^{-5}	2.20776×10^{-7}	-6.83994×10^{-10}	8.45864×10^{-13}
	1700–1400	8.30016×10^{-1}	3.84058×10^{-3}	-4.60296×10^{-5}	2.87215×10^{-7}	-9.06596×10^{-10}	1.13273×10^{-12}
	1400–1250	8.31758×10^{-1}	3.04705×10^{-3}	-3.04947×10^{-5}	1.69431×10^{-7}	-5.11003×10^{-10}	6.40411×10^{-13}
	1250–1100	8.59116×10^{-1}	1.81955×10^{-3}	-1.10266×10^{-5}	3.18110×10^{-8}	-5.87243×10^{-11}	7.75420×10^{-14}
	1100–980	8.61726×10^{-1}	2.86690×10^{-3}	-2.99960×10^{-5}	1.66603×10^{-7}	-4.82577×10^{-10}	5.70288×10^{-13}
	980–800	7.75321×10^{-1}	5.18663×10^{-3}	-7.07737×10^{-5}	4.78996×10^{-7}	-1.57610×10^{-9}	2.00157×10^{-12}
	800–670	6.80093×10^{-1}	8.80242×10^{-3}	-1.24108×10^{-4}	8.56001×10^{-7}	-2.84751×10^{-9}	3.63835×10^{-12}
	670–540	6.25421×10^{-1}	8.52030×10^{-3}	-1.02256×10^{-4}	6.34909×10^{-7}	-1.97938×10^{-9}	2.43387×10^{-12}
	540–400	6.37646×10^{-1}	8.36721×10^{-3}	-1.35457×10^{-4}	1.05003×10^{-6}	-3.76433×10^{-9}	5.04245×10^{-12}
	400–280	4.96556×10^{-1}	1.58356×10^{-2}	-2.22887×10^{-4}	1.53916×10^{-6}	-5.12438×10^{-9}	6.54870×10^{-12}
	280–1	1.92913×10^{-1}	1.33936×10^{-2}	-1.05850×10^{-4}	4.06491×10^{-7}	-7.82327×10^{-10}	6.44872×10^{-13}
Solar radiation (Chou and Suarez 2002)	0.175–0.225	8.17735×10^{-1}	-3.86350×10^{-3}	8.20070×10^{-5}	-6.30772×10^{-7}	2.09174×10^{-9}	-2.53986×10^{-12}
	0.225–0.28	8.19608×10^{-1}	-3.49546×10^{-3}	7.66673×10^{-5}	-5.95807×10^{-7}	1.98534×10^{-9}	-2.41684×10^{-12}
	0.245–0.26	8.19382×10^{-1}	-3.49409×10^{-3}	7.67196×10^{-5}	-5.96401×10^{-7}	1.98758×10^{-9}	-2.41972×10^{-12}
	0.28–0.295	8.21709×10^{-1}	-3.27641×10^{-3}	7.30117×10^{-5}	-5.69531×10^{-7}	1.89932×10^{-9}	-2.31112×10^{-12}
	0.295–0.31	8.23186×10^{-1}	-3.22693×10^{-3}	7.21252×10^{-5}	-5.63121×10^{-7}	1.87855×10^{-9}	-2.28593×10^{-12}
	0.31–0.32	8.24301×10^{-1}	-3.21144×10^{-3}	7.18771×10^{-5}	-5.61753×10^{-7}	1.87568×10^{-9}	-2.28431×10^{-12}
	0.32–0.40	8.24344×10^{-1}	-2.88730×10^{-3}	6.64596×10^{-5}	-5.22422×10^{-7}	1.74526×10^{-9}	-2.12194×10^{-12}
	0.40–0.70	8.07458×10^{-1}	-1.92418×10^{-3}	5.24142×10^{-5}	-4.26803×10^{-7}	1.43657×10^{-9}	-1.74064×10^{-12}
	0.70–1.22	7.78807×10^{-1}	-6.16071×10^{-4}	3.39189×10^{-5}	-3.01533×10^{-7}	1.03259×10^{-9}	-1.24186×10^{-12}
	1.22–2.27	7.40905×10^{-1}	1.53727×10^{-3}	1.02332×10^{-5}	-1.76837×10^{-7}	7.30732×10^{-10}	-9.76048×10^{-13}
	2.27–10.0	8.62046×10^{-1}	2.36942×10^{-3}	-2.03158×10^{-5}	9.20983×10^{-8}	-2.27756×10^{-10}	2.47343×10^{-13}
IR radiation (CH02)	3000–1900	8.39643×10^{-1}	5.62536×10^{-4}	1.80323×10^{-5}	-2.00121×10^{-7}	7.33420×10^{-10}	-9.08561×10^{-13}
	1900–1380	8.29129×10^{-1}	3.81418×10^{-3}	-4.52455×10^{-5}	2.80468×10^{-7}	-8.82475×10^{-10}	1.10158×10^{-12}
	1380–1215	8.41478×10^{-1}	2.44696×10^{-3}	-2.04386×10^{-5}	9.72308×10^{-8}	-2.74135×10^{-10}	3.48659×10^{-13}
	1215–1100	8.59118×10^{-1}	1.82014×10^{-3}	-1.10368×10^{-5}	3.18796×10^{-8}	-5.89274×10^{-11}	7.77626×10^{-14}
	1100–980	8.61726×10^{-1}	2.86689×10^{-3}	-2.99957×10^{-5}	1.66601×10^{-7}	-4.82569×10^{-10}	5.70278×10^{-13}
	980–800	7.75323×10^{-1}	5.18654×10^{-3}	-7.07720×10^{-5}	4.78982×10^{-7}	-1.57605×10^{-9}	2.00149×10^{-12}
	800–620	6.53755×10^{-1}	9.19425×10^{-3}	-1.22649×10^{-4}	8.13286×10^{-7}	-2.63425×10^{-9}	3.30636×10^{-12}
	620–540	6.25421×10^{-1}	8.51559×10^{-3}	-1.02169×10^{-4}	6.34286×10^{-7}	-1.97735×10^{-9}	2.43141×10^{-12}
	540–340	6.12783×10^{-1}	1.01960×10^{-2}	-1.43871×10^{-4}	1.02092×10^{-6}	-3.50022×10^{-9}	4.59169×10^{-12}
	340–0	1.92855×10^{-1}	1.33951×10^{-2}	-1.05833×10^{-4}	4.06128×10^{-7}	-7.80459×10^{-10}	6.41835×10^{-13}

TABLE A4. Values of coefficients in Eq. (4d) for the parameterization of truncation factor f_δ for solar spectral bands when effective particle sizes are below 200 μm.

		Parameterization					
		Coef					
Scheme	Wavelength (μm) or wavenumber (cm^{-1})	Order 0	Order 1	Order 2	Order 3	Order 4	Order 5
Solar radiation (EB)	0.25–0.7	-6.48876×10^{-2}	4.83353×10^{-3}	-1.33483×10^{-5}	-1.23241×10^{-7}	7.08835×10^{-10}	-9.97161×10^{-13}
	0.7–1.3	-9.75375×10^{-2}	5.87070×10^{-3}	-2.69395×10^{-5}	-3.52202×10^{-8}	4.30071×10^{-10}	-6.54365×10^{-13}
	1.3–1.9	-1.11170×10^{-1}	5.65984×10^{-3}	-1.96239×10^{-5}	-1.13629×10^{-7}	7.66787×10^{-10}	-1.16253×10^{-12}
	1.9–2.5	-7.99685×10^{-2}	2.18624×10^{-3}	4.66121×10^{-5}	-6.57481×10^{-7}	2.77534×10^{-9}	-3.90402×10^{-12}
	2.5–3.5	-2.12637×10^{-2}	-6.76446×10^{-5}	3.60037×10^{-5}	-4.08872×10^{-7}	1.66310×10^{-9}	-2.33161×10^{-12}
Solar radiation (Fu and Liou 1993; Fu 1996)	0.2–0.7	-6.47624×10^{-2}	4.82958×10^{-3}	-1.32889×10^{-5}	-1.23681×10^{-7}	7.10394×10^{-10}	-9.99260×10^{-13}
	0.7–1.3	-9.75375×10^{-2}	5.87070×10^{-3}	-2.69395×10^{-5}	-3.52202×10^{-8}	4.30071×10^{-10}	-6.54365×10^{-13}
	1.3–1.9	-1.11170×10^{-1}	5.65984×10^{-3}	-1.96239×10^{-5}	-1.13629×10^{-7}	7.66787×10^{-10}	-1.16253×10^{-12}
	1.9–2.5	-7.99685×10^{-2}	2.18624×10^{-3}	4.66121×10^{-5}	-6.57481×10^{-7}	2.77534×10^{-9}	-3.90402×10^{-12}
	2.5–3.5	-2.12637×10^{-2}	-6.76446×10^{-5}	3.60037×10^{-5}	-4.08872×10^{-7}	1.66310×10^{-9}	-2.33161×10^{-12}
	3.5–4.0	-1.48354×10^{-5}	9.88889×10^{-7}	-2.20182×10^{-8}	2.07062×10^{-10}	-8.19530×10^{-13}	1.14857×10^{-15}
Solar radiation (Chou and Suarez 2002)	0.175–0.225	-3.78813×10^{-2}	4.03464×10^{-3}	-1.28826×10^{-6}	-2.13772×10^{-7}	1.03513×10^{-9}	-1.44250×10^{-12}
	0.225–0.28	-4.07918×10^{-2}	4.04150×10^{-3}	-1.23958×10^{-6}	-2.13159×10^{-7}	1.02702×10^{-9}	-1.42382×10^{-12}
	0.245–0.26	-4.20376×10^{-2}	4.09103×10^{-3}	-2.09214×10^{-6}	-2.06348×10^{-7}	1.00183×10^{-9}	-1.38907×10^{-12}
	0.28–0.295	-4.35756×10^{-2}	4.09999×10^{-3}	-2.31541×10^{-6}	-2.03211×10^{-7}	9.85227×10^{-10}	-1.36045×10^{-12}
	0.295–0.31	-4.53356×10^{-2}	4.16434×10^{-3}	-3.46399×10^{-6}	-1.93803×10^{-7}	9.49853×10^{-10}	-1.31114×10^{-12}
	0.31–0.32	-4.61995×10^{-2}	4.17534×10^{-3}	-3.39066×10^{-6}	-1.95811×10^{-7}	9.60624×10^{-10}	-1.32897×10^{-12}
	0.32–0.40	-5.37547×10^{-2}	4.43434×10^{-3}	-7.25515×10^{-6}	-1.67970×10^{-7}	8.64816×10^{-10}	-1.20340×10^{-12}
	0.40–0.70	-6.76131×10^{-2}	4.93017×10^{-3}	-1.48176×10^{-5}	-1.12492×10^{-7}	6.71440×10^{-10}	-9.47793×10^{-13}
	0.70–1.22	-9.63573×10^{-2}	5.84261×10^{-3}	-2.66793×10^{-5}	-3.61804×10^{-8}	4.31007×10^{-10}	-6.53272×10^{-13}
	1.22–2.27	-1.08063×10^{-1}	5.34627×10^{-3}	-1.37998×10^{-5}	-1.61079×10^{-7}	9.42117×10^{-10}	-1.40238×10^{-12}
	2.27–10.0	-2.67689×10^{-2}	-7.84498×10^{-5}	4.62400×10^{-5}	-5.16547×10^{-7}	2.07291×10^{-9}	-2.87284×10^{-12}

TABLE A5. Values of coefficients in Eqs. (4c), (4d), and (5c) for the parameterization of asymmetry factor g and truncation factor f_δ for solar spectral bands and g for IR spectral bands when effective particle sizes are smaller than 40 μm and larger than 200 μm.

		Parameterization					
		Coef					
		Asymmetry factor ($D_e < 40$ μm)		Asymmetry factor ($D_e > 200$ μm)		Truncation factor ($D_e < 200$ μm)	
Scheme	Wavelength (μm) or wavenumber (cm^{-1})	Order 0	Order 1	Order 0	Order 1	Order 0	Order 1
Solar radiation (EB)	0.25–0.7	7.66444×10^{-1}	6.04084×10^{-4}	8.49088×10^{-1}	-1.40966×10^{-5}	2.57419×10^{-1}	-3.01971×10^{-4}
	0.7–1.3	7.45289×10^{-1}	1.18756×10^{-3}	8.55499×10^{-1}	5.80220×10^{-6}	2.57221×10^{-1}	-3.06100×10^{-4}
	1.3–1.9	7.30084×10^{-1}	2.03063×10^{-3}	8.86821×10^{-1}	9.49325×10^{-5}	2.49845×10^{-1}	-3.40822×10^{-4}
	1.9–2.5	7.22203×10^{-1}	2.87449×10^{-3}	9.15564×10^{-1}	7.28910×10^{-5}	2.26836×10^{-1}	-3.68256×10^{-4}
	2.5–3.5	7.37308×10^{-1}	3.96209×10^{-3}	9.45112×10^{-1}	2.35385×10^{-5}	7.98506×10^{-2}	-1.53125×10^{-4}
IR radiation (EB)	4–8	8.36206×10^{-1}	1.98748×10^{-3}	9.58107×10^{-1}	3.07358×10^{-5}	—	—
	8–12.5	7.61046×10^{-1}	3.45129×10^{-3}	9.29140×10^{-1}	1.68465×10^{-5}	—	—
	12.5–20	6.58765×10^{-1}	4.24104×10^{-3}	9.07237×10^{-1}	8.60858×10^{-5}	—	—
	20–35	4.82129×10^{-1}	9.74958×10^{-3}	9.53628×10^{-1}	3.41426×10^{-5}	—	—
	35–200	1.79995×10^{-1}	1.01968×10^{-2}	8.07256×10^{-1}	1.84895×10^{-4}	—	—
Solar radiation (Fu and Liou 1993; Fu 1996)	0.2–0.7	7.66456×10^{-1}	6.03738×10^{-4}	8.49091×10^{-1}	-1.41240×10^{-5}	2.57432×10^{-1}	-3.01941×10^{-4}
	0.7–1.3	7.45289×10^{-1}	1.18756×10^{-3}	8.55499×10^{-1}	5.80220×10^{-6}	2.57221×10^{-1}	-3.06100×10^{-4}
	1.3–1.9	7.30084×10^{-1}	2.03063×10^{-3}	8.86821×10^{-1}	9.49325×10^{-5}	2.49845×10^{-1}	-3.40822×10^{-4}
	1.9–2.5	7.22203×10^{-1}	2.87449×10^{-3}	9.15564×10^{-1}	7.28910×10^{-5}	2.26836×10^{-1}	-3.68256×10^{-4}
	2.5–3.5	7.37308×10^{-1}	3.96209×10^{-3}	9.45112×10^{-1}	2.35385×10^{-5}	7.98506×10^{-2}	-1.53125×10^{-4}
	3.5–4.0	7.67859×10^{-1}	2.30230×10^{-3}	9.33137×10^{-1}	7.44137×10^{-5}	2.00720×10^{-5}	-2.53542×10^{-8}
IR radiation (Fu and Liou 1993; FU)	2200–1900	8.22557×10^{-1}	1.45060×10^{-3}	9.41254×10^{-1}	7.02096×10^{-5}	—	—

TABLE A5. (*Continued*)

Scheme	Wavelength (μm) or wavenumber (cm^{-1})	Parameterization: Coef: Asymmetry factor ($D_e < 40$ μm) Order 0	Asymmetry factor ($D_e < 40$ μm) Order 1	Asymmetry factor ($D_e > 200$ μm) Order 0	Asymmetry factor ($D_e > 200$ μm) Order 1	Truncation factor ($D_e < 200$ μm) Order 0	Truncation factor ($D_e < 200$ μm) Order 1
	1900–1700	8.59605×10^{-1}	1.87723×10^{-3}	9.65780×10^{-1}	1.82339×10^{-5}	—	—
	1700–1400	8.39411×10^{-1}	2.19684×10^{-3}	9.62935×10^{-1}	1.83127×10^{-5}	—	—
	1400–1250	8.36121×10^{-1}	1.97990×10^{-3}	9.57917×10^{-1}	3.11948×10^{-5}	—	—
	1250–1100	8.54217×10^{-1}	1.56394×10^{-3}	9.59508×10^{-1}	3.90148×10^{-5}	—	—
	1100–980	8.65434×10^{-1}	1.83323×10^{-3}	9.73357×10^{-1}	2.55151×10^{-5}	—	—
	980–800	7.60677×10^{-1}	3.45712×10^{-3}	9.29042×10^{-1}	1.68499×10^{-5}	—	—
	800–670	6.88603×10^{-1}	4.90534×10^{-3}	9.29937×10^{-1}	1.30141×10^{-5}	—	—
	670–540	6.69676×10^{-1}	4.26140×10^{-3}	9.18157×10^{-1}	6.10340×10^{-5}	—	—
	540–400	6.28338×10^{-1}	4.73202×10^{-3}	8.32680×10^{-1}	2.55297×10^{-4}	—	—
	400–280	4.64257×10^{-1}	1.00688×10^{-2}	9.51563×10^{-1}	3.27013×10^{-5}	—	—
	280–1	1.79994×10^{-1}	1.01968×10^{-2}	8.07248×10^{-1}	1.84923×10^{-4}	—	—
Solar radiation (Chou and Suarez 2002)	0.175–0.225	7.66691×10^{-1}	-2.00105×10^{-4}	8.18686×10^{-1}	-2.75106×10^{-5}	2.60058×10^{-1}	-2.90477×10^{-4}
	0.225–0.28	7.72021×10^{-1}	-8.15784×10^{-5}	8.28250×10^{-1}	-2.16818×10^{-5}	2.59275×10^{-1}	-2.94909×10^{-4}
	0.245–0.26	7.71766×10^{-1}	-7.81557×10^{-5}	8.28313×10^{-1}	-2.17255×10^{-5}	2.59215×10^{-1}	-2.95401×10^{-4}
	0.28–0.295	7.75803×10^{-1}	-1.27872×10^{-5}	8.33713×10^{-1}	-1.84934×10^{-5}	2.58572×10^{-1}	-2.97089×10^{-4}
	0.295–0.31	7.77173×10^{-1}	1.36140×10^{-5}	8.35533×10^{-1}	-1.74760×10^{-5}	2.58261×10^{-1}	-2.97429×10^{-4}
	0.31–0.32	7.78112×10^{-1}	2.59493×10^{-5}	8.36536×10^{-1}	-1.67437×10^{-5}	2.58047×10^{-1}	-2.97727×10^{-4}
	0.32–0.40	7.79157×10^{-1}	1.66248×10^{-4}	8.42081×10^{-1}	-1.39356×10^{-5}	2.57596×10^{-1}	-2.99031×10^{-4}
	0.40–0.70	7.66409×10^{-1}	6.05103×10^{-4}	8.49101×10^{-1}	-1.41154×10^{-5}	2.57346×10^{-1}	-3.02663×10^{-4}
	0.70–1.22	7.48712×10^{-1}	1.07975×10^{-3}	8.54665×10^{-1}	9.22357×10^{-7}	2.57332×10^{-1}	-3.05940×10^{-4}
	1.22–2.27	7.23795×10^{-1}	2.15086×10^{-3}	8.84575×10^{-1}	7.63038×10^{-5}	2.46870×10^{-1}	-3.38297×10^{-4}
	2.27–10.0	8.67236×10^{-1}	1.57449×10^{-3}	9.68284×10^{-1}	3.27193×10^{-5}	1.08279×10^{-1}	-1.80785×10^{-4}
IR radiation (CH02)	3000–1900	8.22037×10^{-1}	1.45614×10^{-3}	9.41138×10^{-1}	7.03629×10^{-5}	—	—
	1900–1380	8.38577×10^{-1}	2.19062×10^{-3}	9.62621×10^{-1}	1.91023×10^{-5}	—	—
	1380–1215	8.40117×10^{-1}	1.82181×10^{-3}	9.56802×10^{-1}	3.66579×10^{-5}	—	—
	1215–1100	8.54231×10^{-1}	1.56392×10^{-3}	9.59514×10^{-1}	3.90173×10^{-5}	—	—
	1100–980	8.65434×10^{-1}	1.83323×10^{-3}	9.73358×10^{-1}	2.55125×10^{-5}	—	—
	980–800	7.60677×10^{-1}	3.45712×10^{-3}	9.29041×10^{-1}	1.68516×10^{-5}	—	—
	800–620	6.82544×10^{-1}	4.77710×10^{-3}	9.32307×10^{-1}	1.93661×10^{-5}	—	—
	620–540	6.69665×10^{-1}	4.25948×10^{-3}	9.18097×10^{-1}	6.12190×10^{-5}	—	—
	540–340	5.76417×10^{-1}	6.90531×10^{-3}	9.11667×10^{-1}	1.09033×10^{-4}	—	—
	340–0	1.79998×10^{-1}	1.01969×10^{-2}	8.07307×10^{-1}	1.84793×10^{-4}	—	—

schemes, the broadband-averaged scattering properties, including mass extinction coefficient, mass absorption coefficient, single-scattering albedo, and truncation factor, are parameterized as a function of the effective particle size. There are some other radiation schemes available in the GCM weather forecast and climate community that do not use any of these spectral intervals (e.g., Lacis and Hansen 1974, Edwards and Slingo 1996; Mlawer et al. 1997; Iacono et al. 2000). The parameterizations of their radiation schemes can be done in the similar way as those for the EB, FU, and CH99/CH02 schemes. It would be interesting to test the redeveloped parameterization schemes within the framework of Intercomparison of Radiation Codes for Climate Models (Ellingson and Fouquart 1991) or the more recent Continuous Intercomparison of Radiation Codes (Oreopoulos and Mlawer 2009). Our parameterizations incorporate both the abundant ice cloud microphysical data now available and recent advances in deriving single-scattering properties of nonspherical ice particles for the redeveloped parameterizations. In future work, we hope to determine the impact of the redeveloped parameterizations on GCM simulations.

Cloud radiative forcing (CRF) is first derived using a combination of the discrete ordinates radiative transfer model and a line-by-line model that is used to simulate cloud radiative forcing at both the surface and top of the atmosphere (TOA) for different parameterization schemes. The differences in CRF between the FU, CH99/CH02, and EB versions of the redeveloped schemes are generally small, with maximum instantaneous differences of about 5 W m^{-2}. The redeveloped

parameterization schemes are then applied to the radiative transfer models used for climate models. The ice cloud optical and microphysical properties from the Moderate-Resolution Imaging Spectroradiometer (MODIS) cloud product over a granule and the collocated atmospheric profiles from the Atmospheric Infrared Sounder (AIRS) product are input to the radiation models implemented with the three parameterization schemes to compare the differences in CRF between the redeveloped and existing parameterization schemes.

Although differences are small in the LW CRF between the redeveloped and existing parameterization schemes, the differences in the SW CRF are much larger.

- The redeveloped and existing EB parameterization schemes for LW CRF at both the TOA and the surface have negligible differences. Note that, to be consistent with EB LW parameterization schemes used in the CRM, a simplified treatment is used with a diffusivity factor of 1.66 that only takes into account the mass absorption coefficient.
- Distinct differences are found between the redeveloped and existing CH99/CH02 parameterization schemes for LW CRF at the TOA, although the mean values of their differences are around 0 W m^{-2}. The differences at the surface are negligible.
- The LW CRF using FU parameterization schemes has similar features to those of CH99/CH02 parameterization schemes.
- The redeveloped FU parameterization scheme has stronger negative SW CRF at both the TOA and surface.
- The redeveloped CH99/CH02 parameterization scheme leads to a weaker negative SW CRF at the TOA but a stronger positive CRF at the surface. Larger SW absorption in ice clouds has been found.
- With respect to the redeveloped FU and CH99/CH02 parameterization schemes for SW CRF, the redeveloped EB parameterization scheme used in the Column Radiation Model (CRM) has a much weaker influence on SW CRF.

Acknowledgments. This research was supported in part by a NASA Research Grants NNL06AA01A and NNX08AF68G. The authors specifically acknowledge the support and encouragement of Dr. Donald Anderson and Dr. Hal Maring at NASA Headquarters. Dr. Baum's research is supported by NASA Grant NNX08AF81G. This study is also partially supported by the National Science Foundation (NSF) Physical Meteorology Program (ATM-0239605).

APPENDIX

The values of the fitting coefficients in Eqs. (4a)–(4d) and (5a)–(5c) for different parameterization schemes are listed in Tables A1–A5.

REFERENCES

Bailey, M., and J. Hallett, 2004: Growth rates and habits of ice crystals between −20° and −70°C. *J. Atmos. Sci.,* **61,** 514–544.

Baran, A. J., 2004: On the scattering and absorption properties of cirrus cloud. *J. Quant. Spectrosc. Radiat. Transfer,* **89,** 17–36.

Baum, B. A., D. P. Kratz, P. Yang, S. C. Ou, Y. Hu, P. F. Soulen, and S. C. Tsay, 2000a: Remote sensing of cloud properties using MODIS airborne simulator imagery during SUCCESS. 1. Data and models. *J. Geophys. Res.,* **105,** 11 767–11 780.

——, P. F. Soulen, K. I. Strabala, M. D. King, S. A. Ackerman, and W. P. Menzel, 2000b: Remote sensing of cloud properties using MODIS airborne simulator imagery during SUCCESS. 2. Cloud thermodynamic phase. *J. Geophys. Res.,* **105,** 11 781–11 792.

——, A. J. Heymsfield, P. Yang, and S. T. Bedka, 2005a: Bulk scattering properties for the remote sensing of ice clouds. Part I: Microphysical data and models. *J. Appl. Meteor.,* **44,** 1885–1895.

——, P. Yang, A. J. Heymsfield, S. Platnick, M. D. King, Y.-X. Hu, and S. T. Bedka, 2005b: Bulk scattering properties for the remote sensing of ice clouds. Part II: Narrowband models. *J. Appl. Meteor.,* **44,** 1896–1911.

——, ——, S. L. Nasiri, A. K. Heidinger, A. J. Heymsfield, and J. Li, 2007: Bulk scattering properties for the remote sensing of ice clouds. Part III: High-resolution spectral models from 100 to 3250 cm^{-1}. *J. Appl. Meteor. Climatol.,* **46,** 423–434.

Chou, M.-D., and M. J. Suarez, 2002: A solar radiation parameterization for atmospheric studies. NASA Tech. Memo. NASA TM-1999-10460. Vol. 15, 52 pp.

——, ——, C.-H. Ho, M. M.-H. Yan, and K.-T. Lee, 1998: Parameterizations for cloud overlapping and shortwave single-scattering properties for use in general circulation and cloud ensemble models. *J. Climate,* **11,** 202–214.

——, K.-T. Lee, S.-C. Tsay, and Q. Fu, 1999: Parameterization for cloud longwave scattering for use in atmospheric models. *J. Climate,* **12,** 159–169.

——, ——, and P. Yang, 2002: Parameterization of shortwave cloud optical properties for a mixture of ice particle habits for use in atmospheric models. *J. Geophys. Res.,* **107,** 4600, doi:10.1029/2002JD002061.

Dessler, A. E., and P. Yang, 2003: The distribution of tropical thin cirrus clouds inferred from *Terra* MODIS data. *J. Climate,* **16,** 1241–1247.

Draine, B. T., and P. J. Flatau, 1994: Discrete-dipole approximation for scattering calculations. *J. Opt. Soc. Amer.,* **11,** 1491–1499.

Ebert, E. E., and J. A. Curry, 1992: A parameterization of ice cloud optical properties for climate models. *J. Geophys. Res.,* **97,** 3831–3836.

Edwards, J. M., and A. Slingo, 1996: Studies with a flexible new radiation code. I: Choosing a configuration for a large-scale model. *Quart. J. Roy. Meteor. Soc.,* **122,** 689–719.

Ellingson, R. G., and Y. Fouquart, 1991: The intercomparison of radiation codes in climate models: An overview. *J. Geophys. Res.,* **96,** 8925–8927.

Fu, Q., 1996: An accurate parameterization of the solar radiative properties of cirrus clouds for climate models. *J. Climate,* **9,** 2058–2082.

——, and K. N. Liou, 1993: Parameterization of the radiative properties of cirrus clouds. *J. Atmos. Sci.,* **50,** 2008–2025.

——, P. Yang, and W. B. Sun, 1998: An accurate parameterization of the infrared radiative properties of cirrus clouds for climate models. *J. Climate,* **11,** 2223–2237.

Gao, B.-C., K. Meyer, and P. Yang, 2004: A new concept on remote sensing of cirrus optical depth and effective ice particle size using strong water vapor absorption channels near 1.38 and 1.88 μm. *IEEE Trans. Geosci. Remote Sens.,* **42,** 1891–1899.

Hatzianastassiou, N., A. Fotiadi, C. Matsoukas, K. Pavlakis, E. Drakakis, D. Hatzidimitriou, and I. Vardavas, 2004: Long-term global distribution of earth's shortwave radiation budget at the top of atmosphere. *Atmos. Chem. Phys.,* **4,** 1217–1235.

Heidinger, A. K., 1998: Nadir sounding of clouds and aerosol in the A-band of oxygen. Ph.D. dissertation, Colorado State University, 226 pp.

Heymsfield, A. J., and L. M. Miloshevich, 2003: Parameterization for the cross-sectional area and extinction of cirrus and stratiform ice cloud particles. *J. Atmos. Sci.,* **60,** 936–956.

——, A. Bansemer, P. R. Field, S. L. Durden, J. Stith, J. E. Dye, W. Hall, and T. Grainger, 2002: Observations and parameterizations of particle size distributions in deep tropical cirrus and stratiform precipitating clouds: Results from in situ observations in TRMM field campaigns. *J. Atmos. Sci.,* **59,** 3457–3491.

——, S. Matrosov, and B. A. Baum, 2003: Ice water path–optical depth relationships for cirrus and precipitating cloud layers. *J. Appl. Meteor.,* **42,** 1369–1390.

——, A. Bansemer, C. Schmitt, C. Twohy, and M. R. Poellot, 2004: Effective ice particle densities derived from aircraft data. *J. Atmos. Sci.,* **61,** 982–1003.

Hong, G., P. Yang, B.-C. Gao, B. A. Baum, Y. X. Hu, M. D. King, and S. Platnick, 2007a: High cloud properties from three years of MODIS *Terra* and *Aqua* data over the tropics. *J. Appl. Meteor. Climatol.,* **46,** 1840–1856.

——, ——, H.-L. Huang, B. A. Baum, Y. X. Hu, and S. Platnick, 2007b: The sensitivity of ice cloud optical and microphysical passive satellite retrievals to cloud geometrical thickness. *IEEE Trans. Geosci. Remote Sens.,* **45,** 1315–1323.

Huang, H.-L., P. Yang, H. Wei, B. A. Baum, Y. X. Hu, P. Atonelli, and S. A. Ackerman, 2004: Inference of ice cloud properties from high spectral resolution infrared observations. *IEEE Trans. Geosci. Remote Sens.,* **42,** 842–852.

Iacono, M. J., E. J. Mlawer, S. A. Clough, and J.-J. Morcrette, 2000: Impact of an improved longwave radiation model, RRTM, on the energy budget and thermodynamic properties of the NCAR community climate model, CCM3. *J. Geophys. Res.,* **105,** 14 873–14 890.

Key, J. R., P. Yang, B. A. Baum, and S. L. Nasiri, 2002: Parameterization of shortwave ice cloud optical properties for various particle habits. *J. Geophys. Res.,* **107,** 4181, doi:10.1029/2001JD000742.

Kiehl, J. T., J. J. Hack, G. B. Bonan, B. A. Boville, D. L. Williamson, and P. J. Rasch, 1998: The National Center for Atmospheric Research Community Climate Model: CCM3. *J. Climate,* **11,** 1131–1149.

King, M. D., S. Platnick, P. Yang, G. T. Arnold, M. A. Gray, J. C. Riédi, S. A. Ackerman, and K. N. Liou, 2004: Remote sensing of liquid water and ice cloud optical thickness and effective radius in the Arctic: Application of airborne multispectral MAS data. *J. Atmos. Oceanic Technol.,* **21,** 857–875.

——, ——, P. A. Hubanks, G. T. Arnold, E. G. Moody, G. Wind, and B. Wind, 2006: Collection 005 change summary for the MODIS cloud optical property (06_OD) Algorithm. MODIS Collection 005 Change Summary Document, 23 pp.

Kokhanovsky, A. A., Ed., 2006: *Light Scattering Reviews: Single and Multiple Light Scattering*. Springer, 493 pp.

——, and T. Nauss, 2006: Reflection and transmission of solar light by clouds: Asymptotic theory. *Atmos. Chem. Phys.,* **6,** 5537–5545.

Kosarev, A. L., and I. P. Mazin, 1991: An empirical model of the physical structure of upper layer clouds. *Atmos. Res.,* **26,** 213–228.

Lacis, A. A., and J. E. Hansen, 1974: A parametrization for the absorption of solar radiation in the earth's atmosphere. *J. Atmos. Sci.,* **31,** 118–133.

Li, J., C.-Y. Liu, H.-L. Huang, T. J. Schmit, W. P. Menzel, and J. J. Gurka, 2005: Optimal cloud-clearing for AIRS radiances using MODIS. *IEEE Trans. Geosci. Remote Sens.,* **43,** 1266–1278.

Liou, K.-N., 1986: Influence of cirrus clouds on weather and climate processes: A global perspective. *Mon. Wea. Rev.,* **114,** 1167–1199.

——, 1992: *Radiation and Cloud Processes in the Atmosphere: Theory, Observation, and Modeling*. Oxford University Press, 487 pp.

——, and Y. Takano, 1994: Light scattering by nonspherical particles: Remote sensing and climate implications. *Atmos. Res.,* **31,** 271–298.

Liu, G., and J. A. Curry, 1999: Tropical ice water amount and its relations to other atmospheric hydrological parameters as inferred from satellite data. *J. Appl. Meteor.,* **38,** 1182–1194.

Lubin, D., B. Chen, D. H. Bromwich, R. C. J. Somerville, W. H. Lee, and K. M. Hines, 1998: The impact of Antarctic cloud radiative properties on a GCM climate simulation. *J. Climate,* **11,** 447–462.

Lynch, D. K. K. Sassen, D. O. Starr, and G. Stephens, Eds., 2002: *Cirrus*. Oxford University Press, 480 pp.

Macke, A., J. Mueller, and E. Raschke, 1996: Single scattering properties of atmospheric ice crystals. *J. Atmos. Sci.,* **53,** 2813–2825.

——, P.-N. Francis, G. M. McFarquhar, and S. Kinne, 1998: The role of ice particle shapes and size distributions in the single scattering properties of cirrus clouds. *J. Atmos. Sci.,* **55,** 2874–2883.

McFarquhar, G. M., P. Yang, A. Macke, and A. J. Baran, 2002: A new parameterization of single scattering solar radiative properties for tropical anvils using observed ice crystal size and shape distributions. *J. Atmos. Sci.,* **59,** 2458–2478.

Meyer, K., P. Yang, and B.-C. Gao, 2004: Optical thickness of tropical cirrus clouds derived from the MODIS 0.66 and 1.375-μm channels. *IEEE Trans. Geosci. Remote Sens.,* **42,** 833–841.

Miloshevich, L. M., and A. J. Heymsfield, 1997: A balloon-borne continuous cloud particle replicator for measuring vertical profiles of cloud microphysical properties: Instrument design, performance, and collection efficiency analysis. *J. Atmos. Oceanic Technol.,* **14,** 753–768.

Minnis, P., P. W. Heck, and D. Y. Young, 1993: Inference of cirrus cloud properties using satellite-observed visible and infrared radiances. Part II: Verification of theoretical cirrus radiative properties. *J. Atmos. Sci.,* **50,** 1305–1322.

Mishchenko, M. I., L. D. Travis, and D. W. Mackowski, 1996: T-matrix computations of light scattering by nonspherical particles: A review. *J. Quant. Spectrosc. Radiat. Transfer,* **55,** 535–575.

——, J. W. Hovenier, and L. D. Travis, 2000: *Light Scattering by Nonspherical Particles: Theory, Measurements, and Applications*. Academic Press, 690 pp.

——, L. D. Travis, and A. A. Lacis, 2002: *Scattering, Absorption, and Emission of Light by Small Particles*. Cambridge University Press, 445 pp.

Mitchell, D. L., 2002: Effective diameter in radiation transfer: General definition, applications, and limitations. *J. Atmos. Sci.,* **59,** 2330–2346.

——, and W. P. Arnott, 1994: A model predicting the evolution of ice particle size spectra and radiative properties of cirrus clouds. Part II: Dependence of absorption and extinction on ice crystal morphology. *J. Atmos. Sci.,* **51,** 817–832.

Mlawer, E. J., S. J. Taubman, P. D. Brown, M. J. Iacono, and S. A. Clough, 1997: Radiative transfer for inhomogeneous atmospheres: RRTM, a validated correlated-k model for the longwave. *J. Geophys. Res.,* **102,** 16 663–16 682.

Morcrette, J. J., and C. Jakob, 2000: The response of the ECMWF model to changes in the cloud overlap assumption. *Mon. Wea. Rev.,* **128,** 1707–1732.

Olsen, E. T., and Coauthors, 2007: AIRS version 5 release level 2 standard product quick start. Version 1.1, Jet Propulsion Laboratory, California Institute of Technology, 67 pp.

Oreopoulos, L., and E. Mlawer, 2009: The Continual Intercomparison of Radiation Codes (CIRC): Assessing anew the quality of GCM radiation algorithms. *Bull. Amer. Meteor. Soc.,* in press.

——, M.-D. Chou, M. Khairoutdinov, H. W. Barker, and R. F. Cahalan, 2004: Performance of Goddard Earth Observing System GCM column radiation models under heterogeneous cloud conditions. *Atmos. Res.,* **72,** 365–382.

——, S. Platnick, G. Hong, P. Yang, and R. F. Cahalan, 2009: The shortwave radiative forcing bias of liquid and ice clouds from MODIS observations. *Atmos. Chem. Phys.,* **9,** 5865–5875.

Platnick, S., M. D. King, S. A. Ackerman, W. P. Menzel, B. A. Baum, J. C. Riédi, and R. A. Frey, 2003: The MODIS cloud products: Algorithms and examples from Terra. *IEEE Trans. Geosci. Remote Sens.,* **41,** 459–473.

Rossow, W. B., and R. A. Schiffer, 1999: Advances in understanding clouds from ISCCP. *Bull. Amer. Meteor. Soc.,* **80,** 2261–2287.

Stamnes, K., S.-C. Tsay, W. Wiscombe, and K. Jayaweera, 1988: Numerical stable algorithm for discrete-ordinate-method radiative transfer in multiple scattering and emitting layered media. *Appl. Opt.,* **27,** 2502–2509.

Starr, D. O., 1987: A cirrus-cloud experiment: Intensive field observations planned for fire. *Bull. Amer. Meteor. Soc.,* **68,** 119–124.

——, and S. K. Cox, 1985: Cirrus clouds. Part II: Numerical experiments on the formation and maintenance of cirrus. *J. Atmos. Sci.,* **42,** 2682–2694.

Stephens, G. L., S.-C. Tsay, P. W. Stackhouse Jr., and P. J. Flatau, 1990: The relevance of the microphysical and radiative properties of cirrus clouds to climate and climate feedback. *J. Atmos. Sci.,* **47,** 1742–1754.

——, and Coauthors, 2002: The Cloudsat mission and the A-Train: A new dimension of space-based observations of clouds and precipitation. *Bull. Amer. Meteor. Soc.,* **83,** 1771–1790.

Stith, J. L., J. E. Dye, A. Bansemer, A. J. Heymsfield, D. A. Grainger, W. A. Petersen, and R. Cifelli, 2002: Microphysical observations of tropical clouds. *J. Appl. Meteor.,* **41,** 97–117.

——, J. A. Haggerty, A. J. Heymsfield, and C. A. Grainger, 2004: Microphysical characteristics of tropical updrafts in clean conditions. *J. Appl. Meteor.,* **43,** 779–794.

Sun, W., Q. Fu, and Z. Chen, 1999: Finite-difference time domain solution of light scattering by dielectric particles with a perfectly matched layer absorbing boundary condition. *Appl. Opt.,* **38,** 3141–3151.

Takano, Y., and K.-N. Liou, 1989: Solar radiative transfer in cirrus clouds. Part I. Single-scattering and optical properties of hexagonal ice crystals. *J. Atmos. Sci.,* **46,** 3–19.

Toon, O. B., and R. C. Miake-Lye, 1998: Subsonic aircraft: Contrail and cloud effects special study (SUCCESS). *Geophys. Res. Lett.,* **25,** 1109–1112.

Wei, H., P. Yang, J. Li, B. A. Baum, H.-L. Huang, S. Platnick, Y. Hu, and L. Strow, 2004: Retrieval of semitransparent ice cloud optical thickness from Atmospheric Infrared Sounder (AIRS) measurements. *IEEE Trans. Geosci. Remote Sens.,* **42,** 2254–2267.

Wendisch, M., and Coauthors, 2005: Impact of cirrus crystal shape on solar spectral irradiance: A case study for subtropical cirrus. *J. Geophys. Res.,* **110,** D03202, doi:10.1029/2004JD005294.

——, P. Yang, and P. Pilewskie, 2007: Effects of ice crystal habit on thermal infrared radiative properties and forcing of cirrus. *J. Geophys. Res.,* **112,** D08201, doi:10.1029/2006JD007899.

Wylie, D. P., D. L. Jackson, W. P. Menzel, and J. J. Bates, 2005: Trends in global cloud cover in two decades of HIRS observations. *J. Climate,* **18,** 3021–3031.

Wyser, K., and P. Yang, 1998: Average crystal size and bulk shortwave single-scattering properties in ice clouds. *Atmos. Res.,* **49,** 315–335.

Yang, P., and K. N. Liou, 1996a: Geometric-optics–integral-equation method for light scattering by nonspherical ice crystals. *Appl. Opt.,* **35,** 6568–6584.

——, and ——, 1996b: Finite-difference time domain method for light scattering by small ice crystals in three-dimensional space. *J. Opt. Soc. Amer.,* **13,** 2072–2085.

——, ——, K. Wyser, and D. Mitchell, 2000: Parameterization of the scattering and absorption properties of individual ice crystals. *J. Geophys. Res.,* **105,** 4699–4718.

——, B. A. Baum, A. J. Heymsfield, Y. X. Hu, H.-L. Huang, S.-C. Tsay, and S. Ackerman, 2003: Single-scattering properties of droxtals. *J. Quant. Spectrosc. Radiat. Transfer,* **79-80,** 1159–1180.

——, H. Wei, H.-L. Huang, B. A. Baum, Y. X. Hu, G. W. Kattawar, M. I. Mishchenko, and Q. Fu, 2005: Scattering and absorption property database for nonspherical ice particles in the near-through far-infrared spectral region. *Appl. Opt.,* **44,** 5512–5523.

——, L. Zhang, G. Hong, S. L. Nasiri, B. A. Baum, H.-L. Huang, M. D. King, and S. Platnick, 2007: Differences between collection 4 and 5 MODIS ice cloud optical/microphysical products and their impact on radiative forcing simulations. *IEEE Trans. Geosci. Remote Sens.,* **45,** 2886–2899.

Yee, S. K., 1966: Numerical solution of initial boundary value problems involving Maxwell's equations in isotropic media. *IEEE Trans. Antennas Propag.,* **14,** 302–307.

Yurkin, M. A., V. P. Maltsev, and A. G. Hoekstra, 2007: The discrete dipole approximation for simulation of light scattering by particles much larger than the wavelength. *J. Quant. Spectrosc. Radiat. Transfer,* **106,** 546–557.

Zhang, Z., P. Yang, G. W. Kattawar, S.-C. Tsay, B. A. Baum, Y. X. Hu, A. J. Heymsfield, and J. Reichardt, 2004: Geometric optics solution for the scattering properties of droxtal ice crystals. *Appl. Opt.,* **43,** 2490–2499.